Efferocytosis of SARS-CoV-2-infected dying cells impairs macrophage anti-inflammatory functions and clearance of apoptotic cells

Ana C. G. Salina[1†], Douglas dos-Santos[1†], Tamara S. Rodrigues[1†], Marlon Fortes-Rocha[1], Edismauro G. Freitas-Filho[1], Daniel L. Alzamora-Terrel[1], Mikhael H. F. de Lima[2], Daniele C. Nascimento[2], Ícaro M. S. Castro[3], Camila M. Silva[2], Juliana E. Toller-Kawahisa[2], Amanda Becerra[1], Samuel Oliveira[1], Diego B. Caetité[2], Leticia Almeida[1,4], Adriene Y. Ishimoto[1], Thais M. Lima[1], Ronaldo B. Martins[1], Flavio Veras[2], Natália B. do Amaral[5], Marcela C. Giannini[5], Letícia P. Bonjorno[5], Maria I. F. Lopes[5], Maira N. Benatti[7], Sabrina S. Batah[7], Rodrigo C. Santana[5], Fernando C. Vilar[5], Maria A. Martins[6], Rodrigo L. Assad[5], Sergio C. L. de Almeida[5], Fabiola R. de Oliveira[5], Eurico Arruda Neto[1], Thiago M. Cunha[2,4], José C. Alves-Filho[2,4], Fernando Q. Cunha[2,4], Alexandre T. Fabro[7], Helder I. Nakaya[3,4], Dario S. Zamboni[1,4], Paulo Louzada-Junior[5], Rene D. R. Oliveira[5], Larissa D. Cunha[1]*

[1]Departamento de Biologia Celular e Molecular e Bioagentes Patogênicos, Faculdade de Medicina de Ribeirão Preto, Universidade de São Paulo, Ribeirão Preto, SP, Brazil.
[2]Departamento de Farmacologia, Faculdade de Medicina de Ribeirão Preto, Universidade de São Paulo, Ribeirão Preto, São Paulo, Brazil.
[3]Departamento de Análises Clínicas e Toxicológicas, Faculdade de Ciências Farmacêuticas, Universidade de São Paulo, Brazil.
[4]Center of Research in Inflammatory Diseases (CRID), Faculdade de Medicina de Ribeirão Preto, Universidade de São Paulo, Ribeirão Preto, São Paulo, Brazil.
[5]Divisão de Imunologia Clinica, Emergência, Doenças Infecciosas e Unidade de Terapia Intensiva, Faculdade de Medicina de Ribeirão Preto, Universidade de São Paulo, Ribeirão Preto, SP, Brazil.
[6]Departamento de Cirurgia e Anatomia, Faculdade de Medicina de Ribeirão Preto, Universidade de São Paulo, Ribeirão Preto, SP, Brazil.
[7]Departamento de Patologia e Medicina Legal, Faculdade de Medicina de Ribeirão Preto, Universidade de São Paulo, Ribeirão Preto, SP, Brazil.

† A.C.G.S., D.S., and T.S.R. equally contributed to this work.

* Correspondence: Departamento de Biologia Celular e Molecular e Bioagentes Patogênicos
Faculdade de Medicina de Ribeirão Preto, Universidade de São Paulo
Av. Bandeirantes 3900, Ribeirão Preto, SP 14049-900, Brazil
Tel: +55 16 33153319
larissacunha@usp.br
(ORCID iD: 0000-0002-1290-0263),

Abstract

COVID-19 is a disease of dysfunctional immune responses, but the mechanisms triggering immunopathogenesis are not established. The functional plasticity of macrophages allows this cell type to promote pathogen elimination and inflammation or suppress inflammation and promote tissue remodeling and injury repair. During an infection, the clearance of dead and dying cells, a process named efferocytosis, can modulate the interplay between these contrasting functions. Here, we show that engulfment of SARS-CoV2-infected apoptotic cells (AC) exacerbates inflammatory cytokine production, inhibits the expression of efferocytic receptors, and impairs continual efferocytosis by macrophages. We also provide evidence supporting that monocytes and macrophages from severe COVID-19 patients have compromised efferocytic capacity. Our findings reveal that dysfunctional efferocytosis of SARS-CoV-2-infected cell corpses suppress macrophage anti-inflammation and efficient tissue repair programs and provide mechanistic insights for the excessive production of pro-inflammatory cytokines and accumulation of tissue damage associated with COVID-19 immunopathogenesis.

KEYWORDS: COVID-19, macrophage, macrophage polarization, efferocytosis, hyperinflammation, tissue repair

Introduction

Because of its recent emergence, the pathogenesis of COVID-19 is still poorly defined. Patients with severe disease can progress to pneumonia, development of acute respiratory distress syndrome (ARDS) and respiratory failure, septic shock, and multiorgan dysfunction (Siddiqi and Mehra, 2020). These clinical manifestations of the disease have been associated with a dysregulated host immune response and compromised function of the myeloid compartment, suggesting that hyperinflammation and unresolved tissue damage could both contribute to the pathogenesis of severe COVID-19 (Blanco-Melo et al., 2020; Lucas et al., 2020; Rodrigues et al., 2020; Schulte-Schrepping et al., 2020; Silvin et al., 2020; Valle et al., 2020; Veras et al., 2020).

Macrophages and monocytes promote disease tolerance and resolution of inflammation by sensing pathogen and host-derived pathogenic signals and programming their gene expression toward an anti-inflammatory, pro-resolution, and wound-healing phenotype (Martins et al., 2019). This host-protective programming reduces inflammatory cytokine production by other immune and non-immune cells and promotes the repair of damaged tissue to sustain physiological function and re-establish homeostasis (Murray and Wynn, 2011). During the repair process, the efficient clearance of dying cells prevents further tissue dysfunction caused by uncontrolled cytotoxicity and the release of damage-associated molecular patterns (DAMP). Defects in sensing, ingesting, and degradation of dead and dying cells through efferocytosis cause chronic inflammation and autoimmune diseases (Boada-Romero et al., 2020). In addition to preventing the deleterious effects of secondary necrosis, efferocytosis also couples corpse

internalization to other environmental cues (such as local cytokines and metabolites) to temporally and spatially regulate macrophage anti-inflammatory and tissue repair functions (A-Gonzalez et al., 2017; Bosurgi et al., 2017; Perry et al., 2019). While the clearance of apoptotic cells is often associated with alternative macrophage programming, the identity of the dying cell, the type of cell death, and the context of death (either sterile or infectious) can modulate the nature of the macrophage response (Rothlin et al., 2020).

While infection with SARS-CoV2 induces the recruitment of immune cells to the lungs, their role in host defense and the causes for the dysfunction during disease progression remain elusive. Here, we sought to determine how macrophages operate when responding to dying epithelial cells infected with SARS-CoV-2. We found that the presence of viable SARS-CoV-2 in cell corpses dysregulates macrophage anti-inflammatory responses to the efferocytosis of apoptotic cells, promoting excessive production of inflammatory IL-6 and IL-1β while disrupting the efficient continual clearance of dead cells required for effective tissue repair. We also provide evidence that the expression of efferocytic genes is reduced in macrophages from severe COVID-19 patients and that monocytes from hyperinflammatory patients are also less efficient in the clearance of apoptotic cells. Therefore, SARS-CoV-2 infection and the clearance of infected dying cells disrupt macrophage host-protective functions associated with immunopathological manifestations of COVID-19.

Results

Macrophages engulf dying cells carrying viable SARS-CoV-2

SARS-CoV-2 infection causes cytopathic effects in human and primate epithelial cells (Chu et al., 2020; Zhu et al., 2020), possibly mediated by activation of multiple cell death pathways (Chan et al., 2020; Shaohua Li et al., 2020; Shufen Li et al., 2020; Mulay et al., 2021; Ren et al., 2020; Zhu et al., 2020) . Notably, inhibition of apoptosis ameliorates cytokine expression and tissue damage in the lungs of SARS-CoV-2-infected mice, indicating that apoptosis in the lungs is pathogenic (Chu et al., 2021). Immunofluorescent labeling of active caspase-3 in lung tissues of deceased COVID-19 patients confirmed the induction of apoptosis in pseudostratified epithelia, type I and II pneumocytes infected with replicant SARS-CoV2 (**Fig. 1A**, and **Fig. S1A**). Examination of lung tissues also revealed evidence of macrophages with internalized epithelial cells and SARS-CoV-2, suggesting the uptake of infected epithelial cells by macrophages (**Fig. 1B**). Consistent with previous reports (Chu et al., 2020; Ren et al., 2020; Zhu et al., 2020), infection with SARS-CoV-2 induced apoptosis in immortalized epithelial cell lines (both human lung epithelial Calu-3 and simian kidney epithelial Vero CCL81 cells), as shown by annexin V staining (**Fig 1C** and **Fig. S1B**) and caspase-3 activation (**Fig. 1D**). We performed the Median Tissue Culture Infection Dose (TCID50) assay and found that viral particles obtained from isolated apoptotic Vero and Calu-3 cells induced cytopathic effect to an equivalent extent as those released in the culture supernatants (**Fig. S1C**). Furthermore, we isolated annexin V-labelled apoptotic cells (AC) from SARS-CoV-2-infected cell culture and confirmed that they carry viable viral particles (**Fig. 1E**). Therefore, viable SARS-CoV-2 is retained within infected, apoptotic epithelial cells.

Exposure of phosphatidylserine (PtdSer) on the outer plasma membrane of cells undergoing regulated cell death (RCD), as observed by annexin V binding to infected dying cells (**Fig. 1B**), is the most ubiquitous signal that triggers their phagocytosis (Fadok et al., 1992; Nagata, 2018). To determine whether phagocytes efficiently engulf SARS-CoV-2-infected apoptotic cells (Cov2-AC), we used flow cytometry to assess their uptake by primary human macrophages and macrophages differentiated from THP-1 monocytes. We observed that macrophages efficiently engulf CoV2-AC, similarly to the uptake of sterile, UV-irradiated apoptotic cells (UV-AC) (**Fig. 1F and Fig. 1SD**). Analysis by confocal microscopy and staining for Spike protein confirmed the presence of SARS-CoV-2 in engulfed cell corpses (**Fig. 1G**). Finally, either stimulation with infected or sterile dying cells did not robustly affect macrophages viability up to 24 h post-treatment (**Fig. S1E**).

These results demonstrate that macrophages engulf cell corpses carrying viable particles of SARS-CoV-2, offering a framework to investigate their effects on macrophage function.

Efferocytosis of SARS-CoV-2-infected dying cells impairs macrophage anti-inflammatory function

We next addressed the effect of the engulfment of SARS-CoV-2-infected apoptotic cells in macrophages. The uptake of sterile apoptotic cells often promotes macrophage functional polarization toward an anti-inflammatory and tissue repair phenotype (Doran et al., 2020). We first observed that stimulation of primary monocyte-derived macrophages with CoV-2-AC, but not infection with SARS-CoV-2, consistently reduced the expression of genes associated with

alternative programming to tissue remodeling and secretion of immune-modulatory mediators such as *CCL18*, *CD206* (also known as *MRC1*), *MMP9*, *PPARγ* and *CD163* (**Fig. 2A**). Furthermore, stimulation with UV-irradiated apoptotic Vero cells (UV-AC) increased both gene (**Fig. 2A**) and protein (**Fig. 2B, Fig. S2A**) expression of the anti-inflammatory marker CD206. However, upregulation of MRC1 at the gene or protein levels did not occur in response to stimulation with CoV2-AC (**Fig. 2A and B**). We obtained similar results in THP1-derived macrophages stimulated with CoV2-AC obtained from either Calu-3 or Vero cells infected with SARS-CoV-2 (**Fig. S2B-D**). Stimulation with the conditioned supernatants of infected dying cells (containing putative DAMP, cytokines produced by epithelial cells, extracellular vesicles, and released virions) or direct infection with SARS-CoV-2 did not induce *MRC1* transcription (**Fig. 2A, Fig. S2B**) or translation (**Fig. 2B, Fig. S2C** and **D**) in macrophages. To determine if viral viability was required to modulate CD206 expression by infected apoptotic cells, isolated CoV2-AC were exposed to UV irradiation for virus inactivation (**Fig. S2E**). Notably, macrophages treated with epithelial AC containing inactivated SARS-CoV-2 exhibited increased CD206 surface expression, similar to that of UV-AC (**Fig. 2C**). This finding suggests that viable SARS-CoV-2 actively represses alternative programming carried in dying cells and is not primarily enforced by the type of cell death caused by the infection. Efferocytosis of sterile UV-AC in the presence of SARS-CoV-2 still induced higher expression of CD206 in macrophages (**Fig. 2D**). Therefore, the suppression of the CD206 response required delivery of viral particles within cell corpses to macrophages.

Conversely, the uptake of CoV2-AC, but not UV-AC, significantly increased *IL6* expression in monocyte- and THP-1-derived macrophages (**Fig. 2E** and **Fig. S2F**, respectively). The uptake of

CoV2-AC also induced robust secretion of inflammatory IL-6 and IL-1β, in both primary (**Fig. 2F**) and THP-1-derived macrophages (**Fig. S2G** and **H**). Importantly, we did not detect these cytokines in macrophages stimulated with the cell-free conditioned supernatants, and therefore this effect was not due to immune mediators or viral particles released from infected epithelial cells (**Fig. 2F** and **Fig. S2F-H**). Further, the induction of inflammatory cytokines by SARS-CoV-2-loaded corpses required the presence of viable viral particles, as UV-treatment or paraformaldehyde-fixation of isolated CoV2-AC abrogated IL-6 secretion (**Fig. 2G**). Notably, we did not observe robust production of IL-6 in response to dying epithelial cells infected with Coxsackievirus (**Fig. S2I** and **Fig. 2H**). This result suggests that augmented pro-inflammatory cytokine production is not a universal response of macrophages to the uptake of cell corpses infected with positive single-strand viruses.

To confirm the requirement of recognition and binding of CoV2-AC to promote inflammatory skewing, we stimulated macrophages in the presence of annexin V to mask PtdSer exposed on the surface of the apoptotic cells. In the absence of PtdSer ligation, macrophages did not produce IL-6 in response to CoV2-AC (**Fig. 2I** and **Fig. S2J**). Stimulation of macrophages in the presence of actin depolymerization inducer Cytochalasin D, which allows corpse binding but no internalization, also attenuated IL-6 production (**Fig. 2J**).

Collectively, these findings support that sensing and engulfment of dying cells carrying viable SARS-CoV-2 switch the anti-inflammatory, resolutive programming in response to efferocytosis toward an inflammatory phenotype. The exacerbated cytokine production observed in response

to the efferocytosis of infected cell corpses by macrophages may contribute to the cytokine storm associated with COVID-19 hyperinflammatory syndrome.

Efferocytosis of SARS-CoV-2-infected dying cells suppresses continual clearance of apoptotic cells

Several receptors mediate efferocytosis through recognition of PtdSer on the surface of a dying cell, either by direct binding or through a bridging molecule (Boada-Romero et al., 2020; Penberthy and Ravichandran, 2016). We found that engulfment of CoV2-AC by primary macrophages reduced the transcription of such PtdSer receptors, including the scavenger receptors *CD36* and *SRA-I*, *αVβ5* integrin (*ITGB5*), and T cell immunoglobulin mucin receptor 4 (*TIM4*) and MER proto-oncogene tyrosine kinase (*MERTK*) (**Fig. 3A**). In THP-1-macrophages, we also observed reduced expression of *SRA-I, ITGB5,* and *TIM4* receptors in response to infection with SARS-CoV-2 (**Fig. S2K**). Phagocytes can ingest multiple corpses in subsequent rounds of efferocytosis (Miyanishi et al., 2007; Morioka et al., 2018; Park et al., 2011; Yurdagul et al., 2020). Previous *in vivo* work showed that macrophages must continually remove ACs to promote efficient repair of injury and prevent the accumulation of secondarily necrotic cells (Wang et al., 2017; Yurdagul et al., 2020). To determine if repression of efferocytic receptors affects additional uptake of dying cells, we treated macrophages with CoV2-AC and subsequently fed them with apoptotic human Jurkat cells (Jurkat-AC). We found that the engulfment of SARS-CoV-2-infected corpses suppressed the efferocytosis of other apoptotic cells (**Fig. 3B-D, Fig. S2L**). As infection with SARS-CoV-2 reduced the expression of some efferocytic receptors in THP-1 macrophages (**Fig. S2K**), we also tested if it affected the uptake

of apoptotic cells. Comparatively, infection with SARS-CoV-2 reduced AC clearance to a lower extent than prior uptake of CoV2-AC (**Fig. S2M**). Thus, efferocytosis of SARS-CoV-2-infected dying cells affects the expression of efferocytic receptors and impairs the continual removal of apoptotic cells by macrophages.

Lung monocytes and macrophages of severe COVID-19 patients express reduced levels of efferocytic receptors

To gain insight into the contribution of dysfunctional efferocytosis in COVID-19 pathogenesis, we assessed the expression of efferocytic receptors by immunofluorescence in lung tissues obtained from autopsies of deceased COVID-19 patients. We found a reduction in the protein levels of CD36 in $S1009^{+}$ infiltrating phagocytes in the lungs of COVID-19 patients compared to control tissues (**Fig. 4A**). Phagocytes in the lungs of COVID-19 patients also expressed lower protein levels of MERTK (**Fig. 4B**).

Using publicly available single-cell RNA sequencing (scRNA-seq) data from bronchoalveolar lavage (BAL)(Liao et al., 2020), we performed enrichment analysis using the genes differentially expressed (DEG) in mild and severe COVID-19 patients compared with healthy individuals. We targeted efferocytosis-related gene ontology annotated pathways and customized gene sets based on the literature (Boada-Romero et al., 2020; Penberthy and Ravichandran, 2016) (**Table S1**). Clusters identified as macrophages (Liao et al., 2020) revealed significant repression of gene sets related to efferocytosis in severe patients (**Fig. 4C**). While differences in the comparison between moderate and severe patients were observed in clusters of early infiltrating phagocytes

(S1009^{+} CCL18^{-}), they were more pronounced in mature, putative anti-inflammatory macrophages (S11009^{-} CCL18^{+}). Notably, reassessment on scRNAseq by Ren et al. (2021) showed enrichment in pathways related to efferocytosis for genes repressed in alveolar macrophages which were positive for SARS-CoV-2 RNA compared with those which were negative to the virus (**Fig. 4D**). This finding is consistent with the notion that uptake of infected cells reduces the capacity of macrophages to clear other dead cells. Altogether, these data support that macrophages in the lungs of severe COVID-19 patients may also fail in their efferocytic capacity.

Efferocytosis is impaired in monocytes from hyperinflammatory COVID-19 patients

Because inflammatory mediators can reduce the expression of efferocytic receptors and the uptake of apoptotic cells (Banerjee et al., 2010; Feng et al., 2011; Michlewska et al., 2008; Olagnier et al., 2011; Thorp et al., 2011), we also investigated if COVID-19 manifestation in the efferocytic potential of blood monocytes. We profiled the monocyte population in blood samples from 26 moderate to severe patients on the day of hospitalization (**Table S2**). Assessment of circulating cytokines confirmed higher IL-6, IL-8, IL-10, and IL-1β in this cohort of patients (**Fig. S3A**)(Lucas et al., 2020; Rodrigues et al., 2020). We observed an increase in the absolute numbers of circulating monocytes and the proportion of monocytes among total leukocytes in COVID-19 patients when compared to healthy control (HC) volunteers (**Fig. S3C-D**), as described (Lucas et al., 2020). These cells also expressed less human leukocyte antigen DR isotype (HLA-DR) on their surface (**Fig. S3D**), as described (Lucas et al., 2020; Schulte-Schrepping et al., 2020). We observed changes in monocytes subsets in COVID-19 patients, with

an increase in the percentage of intermediate, inflammatory monocytes ($CD14^{hi}$ $CD16^{+}$) and a reduction in non-classical, anti-inflammatory monocytes ($CD14^{low}$ $CD16^{+}$) that execute efferocytosis more efficiently (**Fig. S3F-H**), similar to other observations (Hamers et al., 2019; Schulte-Schrepping et al., 2020; Silvin et al., 2020). We then assessed the expression of CD36, a lipid-binding receptor with an affinity for anionic phospholipids such as PtdSer exposed on dying cells (Parks et al., 2013; Tait and Smith, 1999), and found reduced surface expression on $CD14^{+}$ monocytes of COVID-19 patients, compared to healthy controls (**Fig. S3I**).

We next recovered the PBMC blood fraction from 42 COVID-19 patients by density gradient separation and evaluated the expression of efferocytic receptors by qPCR (**Tables S2**). We found a reduced transcription of *CD36*, *SRA-I*, *ITGB5,* and *TIMD4*, but not *MERTK*, in PBMC from COVID-19 patients compared to HC (**Fig. 4E**). Importantly, such a pattern was not observed in PMBC isolated from the blood of patients with acute respiratory distress syndrome unrelated to COVID-19 (**Table S3**) and admitted to the same hospital facility at the time of this study (**Fig. 4F**). We then addressed a possible association between the levels of efferocytic receptors (**Fig. 4E**) and the worsening of COVID-19. To that end, we stratified these COVID-19 patients according to their hyperinflammatory state at hospital admission, based on a score of clinical criteria (fever, macrophage activation, hematological dysfunction, coagulopathy, hepatic injury, and cytokinaemia) that defines COVID-19-associated hyperinflammation (cHIS score) (Webb et al., 2020). We found a statistically significant reduction in the expression of *CD36*, *TIMD4,* and *SRA-I* for patients with a cHIS score of at least 2, which is associated with worsening in severity and risk of death (Webb et al., 2020) (**Fig. 4G**).

Finally, we assessed the uptake of dying cells by monocytes from COVID-19 patients. We stimulated monocytes obtained from PBMC samples from COVID-19 patients with apoptotic cells and evaluated their phagocytic activity by epifluorescence microscopy. We found that monocytes from COVID-19 patients with cHIS score > 2 were less efficient in the uptake of dying cells (**Fig. 4H**). This failure was not caused by an intrinsic defect in phagocytosis, as monocytes from HC and COVID-19 patients internalized zymosan similarly (**Fig. S3J**).

Thus, monocytes from severe COVID-19 patients that develop hyperinflammation express lower levels of efferocytic receptors and are less efficient in the clearance of dying cells.

Discussion

In summary, we demonstrate that the sensing and engulfment of SARS-CoV-2-infected dying cells by macrophages switches the effector response to efferocytosis from a potential wound healing, anti-inflammatory function to a pro-inflammatory one. Our data supports that the uptake of cell corpses infected with SARS-CoV-2 exacerbates the secretion of inflammatory IL-6 and IL-1β, suggesting a mechanism for the robust secretion of cytokines related to COVID-19 cytokine storm. Another important consequence of this shift in macrophage function is the impairment of macrophage capacity to engulf apoptotic cells continually and promote proper injury resolution. Instead, our data suggest that efferocytosis of infected cells may augment tissue damage by causing inefficient clearance of dead cells. This process may consequently contribute to respiratory complications developed by patients with the severe form of the disease and increase susceptibility to secondary bacterial infections for the lack of effective disease

316 tolerance mechanisms that restrain collateral tissue damage (Jamieson et al., 2013). While such
317 causal connection remains to be investigated, our histological assessment and reanalysis of
318 scRNAseq datasets suggest that the efferocytic capacity of lung macrophages is impaired in the
319 lungs of COVID-19 patients. We further demonstrate that circulating monocytes of COVID-19
320 patients with hyperinflammation present reduced expression of efferocytic receptors and fail to
321 uptake dying cells. While our data is suggestive of a loop between dysfunctional macrophage
322 responses upon the uptake of infected cell corpses in the lungs and signaling affecting efferocytic
323 capacity of blood monocytes, follow-up studies are necessary to establish how COVID-19-
324 associated hyperinflammation impairs the efferocytic machinery in circulating cells. Still,
325 macrophage function in tissue repair and remodeling should be further compromised by the loss
326 of efferocytic potential in infiltrating monocytes.
327
328 In the context of COVID-19 immunopathogenesis, excessive amounts of necrotic cells may lead
329 to high levels of circulating DAMP, such as HMGB1 and lactate dehydrogenase (LDH), both of
330 which correlate with disease severity (Chen et al., 2020; Han et al., 2020; Rodrigues et al., 2020).
331 It is thus possible that the combination of exacerbated cytokine production and interruption of
332 continual efferocytosis in response to engulfment of SARS-CoV-2-infected corpses could both
333 increase the magnitude and duration of inflammation, contributing to the hyperinflammatory
334 state and multiorgan damage in COVID-19. Finally, recent studies reported higher levels of
335 autoantibodies (such as against IFNγ, phospholipids, and annexin A2) in COVID-19 patients
336 (Bastard et al., 2020; Zuniga et al., 2021; Zuo et al., 2020), suggesting that autoantibodies may
337 drive the worsening of the disease. It has long been known that defective engulfment or
338 processing of dying cells causes the development of autoimmune diseases (Boada-Romero et al.,

2020; Cohen et al., 2002; Miyanishi et al., 2007; Peng and Elkon, 2011; Rodriguez-Manzanet et al., 2010). In light of our findings, perhaps defective clearance of apoptotic cells caused by SARS-CoV-2 infection and SARS-CoV-2-loaded ACs also contributes to COVID-19-associated autoimmunity.

As it becomes clear that COVID-19 is a disease of immune dysfunction (Cohen et al., 2002), antivirals, and other therapeutic efforts to limit viral replication may fail to benefit critically ill patients. In those patients, successful therapeutic strategies may rely on targeting dysregulated components of the host response to limit damage to the host, thus promoting disease tolerance and stimulating a resolutive response that restores homeostasis. In this context, our study provides important insights into the mechanisms driving the pathophysiology of COVID-19 that can be explored in the design of therapeutics approaches toward harnessing innate immune responses and macrophage function during SARS-CoV-2 infection.

Material and Methods

Study approval. The procedures followed in the study were approved by the Research Ethics Committee of Hospital das Clínicas de Ribeirão Preto (CEP-FMRP/USP) and by the National Ethics Committee, Brazil (Comissão Nacional de Ética em Pesquisa (CONEP), protocols 30248420.9.0000.5440 and 39722020.9.0000.5440. Written informed consent was obtained from recruited patients.

Patient samples. A total of 59 patients with COVID-19 and 10 patients with non-COVID-19 acute respiratory distress syndrome admitted in the Hospital das Clínicas de Ribeirão Preto from

April to August 2020 were enrolled in this study. SARS-CoV-2 infection was confirmed by RT-PCR of swab samples, as previously described (Corman et al., 2020). Patients were classified according to their clinical manifestations in (1) mild cases, in which there were mild clinical symptoms and no pneumonia was found in imaging; (2) moderate cases, characterized by fever, respiratory tract symptoms, and pneumonia identifiable by imaging; and (3) severe cases, meaning adults who met any of the following features: arterial partial pressure of oxygen (PaO_2)/oxygen concentration (FiO_2) <300 mm Hg, oxygen saturations at 93% at a rest state and respiratory rate > 30 breaths/min. **Table S2** describes clinical, laboratory, and treatment records of COVID-19 patients. **Table S3** describes clinical, laboratory, and treatment records of non-COVID-19 patients admitted with acute respiratory distress syndrome. Samples from healthy donors tested negative for COVID-19 using RT-PCR or tested negative using serology (specific IgM and IgG antibodies; Asan Easy Test COVID-19 IgM/IgG kits, Asan Pharmaceutical Co.) were used as controls or for isolation of monocytes for in vitro studies.

Isolation of human peripheral blood mononuclear cells, monocyte seeding, and macrophage differentiation. Peripheral blood mononuclear cells (PBMC) from healthy donors and COVID-19 patients were isolated from peripheral blood collected in tubes containing EDTA (BD Vacutainer, BD Biosciences). The samples were centrifuged at 400 *g* for 10 min at room temperature (RT), the plasma was discarded, and the cellular portion was diluted in phosphate-buffered saline (PBS). PBMC were isolated by density–gradient centrifugation using Histopaque-1077 (Sigma-Aldrich). The collected PBMC fraction was treated with ACK lysis buffer to lyse erythrocytes and washed twice with PBS. For qRT-PCR, cell lysis proceeded as described below. To obtain monocyte cultures, PBMC were plated on 24-well plates for 1h in

385 serum-free RPMI 1640 (GIBCO) at 37°C in a 5% CO_2 atmosphere for monocyte adhesion. The
386 cells were then washed three times with PBS, followed by media replenishment with RPMI1640
387 media supplemented with penicillin (10.000 U/mL, GIBCO), streptomycin (10.000 µg/mL,
388 GIBCO), 1% glutamine (GIBCO), and 10% heat-inactivated human serum (Sigma Aldrich). For
389 macrophages differentiation, monocytes were cultivated for 7 d in RPMI 1640 supplemented
390 with human serum.
391
392 **Cell Lines.** Calu-3, Vero CCL81, Jurkat, and THP-1 cells were from (ATCC®). Calu-3 and Vero
393 CCL81 cells were maintained in DMEM with 4.5 g/L glucose (GIBCO) supplemented with
394 penicillin (10.000 U/mL), streptomycin (10.000 µg/mL), and 10% heat-inactivated fetal bovine
395 serum (FBS, GIBCO) (DMEMc) at 37°C in a 5% CO_2 atmosphere. Jurkat cells and THP-1 cells
396 were maintained in RPMI1640 media supplemented with penicillin (10.000 U/mL), streptomycin
397 (10.000 µg/mL), 1% glutamine, and 10% FBS (RPMIc) at 37°C in a 5% CO_2 atmosphere.
398
399 THP-1-derived macrophages were obtained by treatment with phorbol 12-myristate 13-acetate
400 (PMA, 50 ng/mL, Sigma-Aldrich) for 24 h, followed by media replenishment with fresh RPMIc
401 and other 24 h incubation period before stimulation.
402 Cell lines were routinely screened for mycoplasma contamination, and all cell lines tested
403 negative.
404
405 **Viral stock.** The SARS-CoV-2 strain (Brazil/SPBR-02/2020) was isolated from the first
406 Brazilian case of COVID-19. The viral stock was produced in a monolayer of Vero CCL81 cells
407 maintained in serum-free DMEM at 37°C in a 5% CO_2 atmosphere. Coxsackievirus B5

(Coxsackie) was originally shared by Dr. Roger M. Loria (Virginia Commonwealth University, Richmond, Virginia, USA) (Gomes et al., 2009). The viral stock was produced in a monolayer of HeLa cells maintained in DMEM supplemented with 2% FBS at 37°C and 5% CO_2. Viral stocks were propagated under BSL3 conditions and stored at -80°C. Viral loads were estimated by titration in Vero CCL81 cells seeded onto 96-well plates and standard limiting dilution to confirm the 50% tissue culture infectious dose.

Isolation of apoptotic cells. To generate SARS-CoV-2-infected apoptotic cells (CoV2-AC) from Vero CCL81 and Calu-3 cultures, or Coxsackievirus B5-infected apoptotic cells (Coxsackie-AC) from Vero CCL81 cultures, cell monolayers were rinsed with PBS, replenished with a thin layer of serum-free media, and infection with a freshly thawed virus aliquot at a multiplicity of infection (MOI) of approximately 0.05 was carried out for 1 h at 37°C and 5% CO_2 for viral adsorption. The cells were then topped with fresh media and incubated for 48 h. Sterile apoptotic cells (UV-AC) were generated by exposure to UV-C radiation (Calu-3 cells at 500 mJ/cm^2 and Vero CCL81 cells at 350 mJ/cm^2) in a UV crosslinker (Fisher Scientific), followed by 6h incubation in DMEMc at 37°C and 5% CO_2. At the established time points, the supernatants were collected and temporarily stored for further processing. Then, a suspension containing CoV2-AC or UV-AC was obtained by carefully pipetting fresh media up and down the plate surface and collecting loosely attached cells. Following spun at 300 *g* for 5 min, pelleted AC were washed with PBS, resuspended in fresh media, and counted with a Neubauer chamber prior to incubation with macrophages.

For virus inactivation, isolated AC suspension was placed onto tissue culture hood surface with an open lid for 20 min with the UV-C lamp on. Virus inactivation was confirmed by $TCID_{50}$, as described below. Alternatively, isolated AC were fixed with 2% paraformaldehyde (PFA) in PBS for 10 min and washed twice with PBS before adding to macrophage cultures.

To prepare the cell-free conditioned supernatants of the infected AC (CoV2-AC Sup), collected supernatants were spun at 300 *g* for 5 min to remove cellular debris; the resulting supernatant was filtered using a 0.22 μm syringe filter and immediately used for macrophage stimulation. The volume of CoV2-AC Sup used to stimulate macrophages was normalized to the amount of collected AC.

Cell death assays. Cells were collected 48 hours post-infection or 6 hours post-irradiation, spun at 300 *g* for 5 min, washed with PBS, and resuspended in the appropriate buffer before labeling.

Detection of PtdSer was performed by annexin-V labeling (APC annexin-V, BD Biosciences, 1:100). 10^6 cells were resuspended in annexin V binding buffer (0.01M HEPES, 0.14M NaCl, 2.5 mM CaCl2, pH 7.4), and labeling was carried out for 15 min on ice. The cells were then fixed with 2% PFA in binding buffer for 10 min and washed before flow cytometric analyses.

For the analysis of cleaved caspase-3, infection of Calu-3 cells was carried out in the presence of Z-VAD-FMK (Selleckchem, Houston, USA) at 20 μM, or mock treatment with vehicle (DMSO), added to cell cultures after virus adsorption. 10^6 collected cells were washed with PBS, and fixation, permeabilization, and staining were carried out using BD Cytofix/Cytoperm™

Fixation/Permeabilization Kit (BD Biosciences), following the manufacturer's instructions. Immunolabelling of intracellular active caspase-3 was performed with anti-cleaved caspase-3 (Asp175) (Clone 5A1E; #9664; Cell Signaling, 1:400) and secondary donkey anti-rabbit IgG conjugated to Alexa Fluor 488 (AF488, Molecular Probes, 1:2500).

Flow cytometric acquisitions were performed in a FACSVerse (BD Biosciences, San Jose, CA, USA) flow cytometer.

$TCID_{50}$ quantification of viable viral particles. 10^6 isolated CoV2-AC and their equivalent purified conditioned supernatants, obtained as described above, were lysed by snap freeze-and-thaw. To estimate viral load in apoptotic cells isolated by annexin V labeling, all infected cells were collected, centrifuged at 300 *g* for 5 min, followed by magnetic separation with annexin V MicroBeads (Miltenyi Biotec) according to the manufacturer's protocol. 10^6 pre-sorted cells, $annexin^+$ cells, and $annexin^-$ cells were lysed by freeze-and-thaw for quantification. Viral loads were estimated by titration in Vero CCL81 cells seeded onto 96-well plates and expressed as 50% tissue culture infectious dose ($TCID_{50}$). Quantification was performed with the Reed-Muench method and plotted as $TCID_{50}$ units per mL(REED and MUENCH, 1938)

***In vitro* assays with THP-1- and PBMC-derived macrophages.** 10^6 THP-1- and PBMC-derived macrophages seeded on 24-well tissue culture plates were rinsed with warm PBS before stimulation. Macrophage cultures were then topped with UV-AC, CoV2-AC, or Coxsackie-AC resuspended in the appropriate serum-containing macrophage media at a 1:1 ratio. For stimulation with conditioned supernatants, CoV2-AC-Sup were added directly to macrophages

cultures and topped with fresh media for volume adjustment. Infection with SARS-CoV-2 or Coxsackie virus was carried out with virus adsorption at MOI 1 in serum-free media for 1 h before topping with fresh serum-containing media. To block AC ligation and efferocytosis, CoV2-AC were pre-incubated with 0.1 or 0.01 µg/mL of annexin-V (BD Biosciences) following the manufacturer's recommendations prior to incubation with macrophages. To block AC internalization, macrophages were pre-treated for 30 min, and incubation was carried out in the presence of Cytochalasin D (10µM, Sigma). Macrophage cultures were rinsed out 2h after incubation to remove unbound AC, topped with fresh media, and stimulation was carried on up to supernatant collection to dose cytokines. At the time points described in the legend of the figures, macrophages were rinsed at least twice with warm PBS to remove cell debris before proceeding to analysis.

For gene expression analysis by RT-qPCR, rinsed macrophage cultures were lysed in appropriate lysis buffer, as described below, and immediately frozen at -80°C.

To estimate CD206 surface expression, rinsed macrophages were removed with a cell scraper, spun at 300 *g* for 5 min, washed with PBS, followed by incubation with rat serum (1:2000) for 5 min at room temperature (RT) and cell surface staining for 15 minutes at 4°C. Cells were labeled with Zombie Violet™ Fixable Viability Kit (Biolegend) and anti-CD206-FITC antibody (clone 19.2, BD Biosciences). The cells were then fixed with 2% PFA for 10 min and washed before flow cytometric analyses in a FACSVerse (BD Biosciences) flow cytometer.

For immunofluorescence imaging of efferocytosis, human monocyte-derived macrophages

seeded onto 13mm round coverslips were incubated with UV-AC or CoV2-AC labeled with 5 µM CellTrace™ CFSE dye (Thermo Scientific) for 2h. After rinsing out non-engulfed AC, macrophages were fixed for 20 min with PBS 2% PFA at room temperature (RT). Cells were then permeabilized with 0.1% Triton-X-100 in PBS for 10 min at room temperature (RT). Next, cells were rinsed twice in PBS and incubated with PBS 1% bovine serum albumin (BSA) and 5 µg/mL normal donkey IgG (Jackson ImmunoResearch) for 45 min RT prior to overnight (ON) incubation at 4ºC with primary antibodies: rabbit polyclonal anti-SARS-CoV-2 spike glycoprotein antibody (ab272504 – Abcam, 1:1000) and Mouse mAb anti-Rat CD11b (clone OX42; ab1211, Abcam, 1:300) diluted in PBS containing 1% BSA. Next, coverslips were washed with PBS, and the following secondary antibodies were used for immunofluorescence: Next, cells were rinsed thoroughly in PBS and incubated for 30 min at RT with the secondary antibodies diluted in PBS: donkey anti-rabbit IgG F(ab)´$_2$-Alexa 594 (1:1000; Thermo Fisher Scientific) and donkey anti-mouse IgG F(ab)´$_2$-Alexa 647 (1:1000; Thermo Fisher Scientific). Cell nuclei were stained with Hoechst 33342. Cells were then rinsed, and coverslips mounted on glass slides with Fluoromount-G (Invitrogen). Samples were analyzed using a Zeiss LSM 780 laser scanning confocal microscope (Carl Zeiss).

For the engulfment assays by flow cytometry, macrophages were labeled with 5 µM CellTrace™ Violet dye (CTV, Thermo Scientific), according to the manufacturer's recommendations. CellTrace™ Violet (CTV)-labeled macrophages were stimulated with UV-AC or CoV2-AC previously stained with 1 µM CellTrace™ Far Red dye (CTFR, Thermo Scientific), or 5 µM CellTrace™ CFSE dye, as described in the legend of the figures. Following the removal of unbound AC, macrophages were collected with a cell scraper, fixed with 2% PFA for 10 min,

and washed before proceeding with the acquisition by flow cytometry. For the two-round efferocytosis assay, first-round UV-AC and CoV2-AC were labeled with a pH indicator fluorogenic intracellular probe (pHrodo Red AM Intracellular pH Indicator - Thermo Scientific). Second-round apoptotic Jurkat cells (UV-Jurkat) were generated by UV-C irradiation at 20 mJ/cm^2, followed by labeling with 1 µM CTFR and incubation at 37°C and 5% CO_2 for 6h. CTV-labelled THP-1 cells were incubated with pHrodo-UV-AC or pHrodo-CoV2-AC for 18h at a 1:1 ratio. Cells were then rinsed three times with PBS to remove non-engulfed AC, and CTV-labelled Jurkat-AC were added to the culture at a 1:1 ratio for 2h. Macrophage cultures were collected with a cell scraper, washed, fixed with 2% PFA for 10 min, and washed before proceeding with the acquisition by flow cytometry. Flow cytometric acquisition was performed in a FACSVerse (BD Biosciences) flow cytometer.

Phenotyping of blood monocytes. Blood samples from healthy donors and COVID-19 patients were processed for erythrocyte lysis with ACK buffer, followed by incubation with Fc blocking (BD Pharmingen) for 5 min at RT and labelling with monoclonal antibodies for CD14 (clone M5E2; BD Pharmingen™), CD16 (clone ebioCB16(CB16); eBioscience Inc., San Diego; USA), CD36 (clone CB38; BD Pharmingen™), HLA-DR (clone L243; BD Pharmingen™), CD3 (clone SK7; BD Pharmingen™), CD19 (clone 6D5; BD Pharmingen™), CD56 (clone NCAM16.2; BD Pharmingen™) and Fixable Viability Dye eFluor 780 (eBioscience) for 30 min at 4°C. The cells were then washed with PBS and fixed with 2% PFA for 10 min before analyses in a FACSVerse (BD Biosciences) flow cytometer.

***In vitro* efferocytosis assay with monocytes from COVID-19 patients.** 10^6 PBMC from healthy donors or COVID patients were plated onto eight-well chamber slides (Tek Chamber Slide, Thermo Scientific) for monocyte adherence, followed by 24h incubation in RPMI supplemented with 10% heat-inactivated human serum before stimulation. For induction of apoptosis in thymocytes, cells isolated from C57BL/6 mice were resuspended in DMEMc and treated with 20 mJ/cm^2 ultraviolet C irradiation and incubated for 6h at 37°C in a 5% CO_2. Monocytes were incubated with apoptotic thymocytes at 1:5 ratio for 1h or zymosan A particles (Thermo Scientific) at 1:1 ratio for 20 min at 37°C and 5% CO_2. The cells were then washed with PBS at least three times to remove unbound apoptotic cells and zymosan particles, followed by fixation with 4% PFA PBS solution for 15 min and rinsed twice with 0.01% Tween-20 Tris-buffered saline (TBS). After permeabilization (0.1% Triton-X-100 in TBS for 3 min at RT), cells were labeled with phalloidin conjugated to Alexa Fluor 488 (Thermo Scientific) and Hoechst 33342, and coverslips mounted with Fluoromount-G. Immunofluorescence and phase-contrast images were acquired with 40x objective lens of Leica DMI4000B microscope (Leica Microsystems; Heidelberg, Germany). To quantify AC engulfment, monocytes were identified by nuclei morphology and membrane boundary, and AC uptake was enumerated using nuclei fragmentation in the internalized thymocytes and transient F-actin reorganization around the engulfed AC as criteria (Mylvaganam et al., 2021; Satyanarayanan et al., 2019). Quantification was performed by the same researcher blinded to sample identification, and at least 10 fields and minimum 30 cells were counted per sample. Phagocytic index, as a normalization by the average percentage of uptake in control samples, was used to account for inherited differences between experiments performed on different days. The representative images were obtained using a Zeiss LSM 780 laser scanning confocal microscope (Carl Zeiss, Heidelberg, Germany).

Cytokine quantification. IL-6 and IL-1β cytokine levels in macrophage supernatants were evaluated by ELISA assay (R&D Systems, Minneapolis, MN, EUA) or BD™ Cytometric Bead Array (CBA) (#551811, BD Biosciences), as indicated in the legend of the figures, following the manufacturers' recommendations. The cytokine levels in culture supernatants were evaluated by CBA. IL-1β, IL-6, IL-8, IL-10, IL-12, and TNF-α detection in serum from healthy donors and patients with COVID-19 were performed with CBA.

RNA isolation and gene expression analyses. Total RNA extraction of PBMC from healthy donors or COVID-19 patients was performed using PureLink™ RNA Mini Kit (Ambion Inc., ThermoFisher Scientific), following the manufacturer's recommendations. Reverse transcription was performed using the High Capacity cDNA Reverse Transcriptase Kit (Applied Biosystems™, Foster City, USA), following the manufacturer's recommendations.

Total RNA extraction for human monocyte- or THP-1-derived macrophages stimulated *in vitro* was performed using Directzol™ RNA miniPrep Kit (Zymo Research, Irvine, CA, USA), following the manufacturer's recommendations. Reverse transcriptase was performed using M-MLV reverse transcriptase (ThermoFisher Scientific) according to the manufacturer's recommendations.

Gene expression RT-qPCR was performed using SybrGreen Master Mix (Applied Biosystems). RT-qPCR was performed in fast mode, following the manufacturer's recommendations. The

589 evaluation of each gene expression was determined by the comparative CT method. Primer
590 sequences used were:
591

Gene	5' Forward	3' Reverse
CCL18	CTCTGCTGCCTCGTCTATACCT	CTTGGTTAGGAGGATGACACCT
CD163	GCGGGAGAGTGGAAGTGAAAG	GTTACAAATCACAGAGACCGCT
CD36	GGGAAAGTCACTGCGACATG	TGCAATACCTGGCTTTTCTCA
GAPDH	GTCTCCTCTGACTTCAACAGCG	ACCACCCTGTTGCTGTAGCCAA
IL6	GGTACATCCTCGACGGCATCT	GTGCCTCTTTGCTGCTTTCAC
ITGB5	AACCAGAGCGTGTACCAGAA	AGGAGAAGTTGTCGCACTCA
MERTK	CTCTGGCGTAGAGCTATCACT	AGGCTGGGTTGGTGAAAACA
MMP9	TGTACCGCTATGGTTACACTCG	GGCAGGGACAGTTGCTTCT
MRC1	AGCCAACACCAGCTCCTCAAGA	CAAAACGCTCGCGCATTGTCCA
PPARγ	ACCAAAGTGCAATCAAAGTGGA	ATGAGGGAGTTGGAAGGCTCT
SRA-1	GCAGTGGGATCACTTTCACAA	AGCTGTCATTGAGCGAGCATC
TIM4	ACAGGACAGATGGATGGAATA CCC	AGCCTTGTGTGTTTCTGCG

592

593 **Histological analysis**. Ultrasound-guided minimally invasive autopsies for COVID-19 deceased
594 patients were approved by the Research Ethics Committee of Hospital das Clínicas de Ribeirão
595 Preto (CEP, protocol no. 4.089.567). Non-neoplasic sections of lung parenchyma were obtained
596 from lobectomies for lung cancer as a control group (Rodrigues et al., 2020). Paraffin sections
597 from lungs were collected and processed as previously described (Rodrigues et al., 2020).
598 Sections were rinsed in PBS, and the antigen retrieval was performed by incubation of samples
599 with 0.1% trypsin (ThermoFisher Scientific) in PBS at 37ºC for 15 min. Next, sections were
600 rinsed and incubated with Image-iT FX Signal Enhancer (ThermoFisher Scientific) for 30 min at
601 RT. Sections were then rinsed in PBS and incubated for 45 min at RT in PBS containing 0.5%
602 BSA and 5µg/mL normal donkey IgG (Jackson ImmunoResearch).
603

For analysis of active caspase 3, lung sections were labeled with primary antibodies diluted in PBS and incubated overnight ON at 4ºC: rabbit polyclonal anti-human cleaved caspase 3 (Asp175) (Clone 5A1E; #9664; Cell Signaling; 1:1000) and mouse anti-dsRNA (1:1000). Then, sections were rinsed thoroughly in PBS and incubated for 45 min at RT with the secondary antibodies: donkey anti-rabbit IgG conjugated to Alexa 594 (1:500; Thermo Fisher Scientific) and donkey anti-mouse IgG F(ab)´$_2$-Alexa 488 (1:500; Thermo Fisher Scientific) diluted in PBS. Sections were then rinsed, and coverslips mounted with DAPI Fluoromount-G (EM Sciences). For *in situ* efferocytosis analysis, lung sections were labeled with primary antibodies diluted in PBS and incubated overnight ON at 4ºC: mouse mAb anti-human CD68 (Clone KP1; Dako; 1:100), rabbit mAb anti-human cytokeratin 18 (Clone N1N3; GeneTex, 1:500) and anti-Spike (rabbit polyclonal anti-SARS-CoV-2 Spike glycoprotein antibody, ab272504 – Abcam; 1:80) previously conjugated to FITC (FITC Conjugation Kit-Lightning-Link®, Abcam, according to the manufacturer's instructions). Then, sections were rinsed thoroughly in PBS and incubated for 45 min at RT with the secondary antibodies: donkey anti-rabbit IgG conjugated to Alexa 594 (1:500; Thermo Fisher Scientific) and donkey anti-mouse IgG F(ab)´$_2$-Alexa 647 (1:500; Thermo Fisher Scientific) diluted in PBS. Next, sections were incubated for 15 min at RT with Hoechst 33342 (Invitrogen), rinsed in PBS, and mounted on glass slides with Fluoromount-G (Invitrogen). Samples from active caspase 3 and *in situ* efferocytosis experiments were analyzed using an ECLIPSE Ti2 Series microscope (Nikon).

For CD36 or MERTK expression analysis, lung sections were labeled with the primary antibodies diluted in PBS and incubated overnight ON at 4ºC: rabbit polyclonal anti-human CD36 (PA5-81996; 1:100 ThermoFisher Scientific) or rabbit mAb anti-human MERTK (Clone

SR29-07; 1:150; ThermoFisher Scientific) and mouse mAb anti-human calprotectin (Clone MAC387; MA1-81381; 1:100; ThermoFisher Scientific). Then, sections were rinsed thoroughly in PBS and incubated for 45 min at RT with the secondary antibodies donkey anti-rabbit IgG conjugated to Alexa 488 (1:500; Thermo Fisher Scientific) and goat anti-mouse IgG conjugated to Alexa 594 (Jackson ImmunoResearch) diluted in PBS. Sections were then rinsed, and coverslips mounted with DAPI Fluoromount-G. Samples were analyzed using an Olympus BX61 Fluorescence Motorized Slide Scanner Microscope Pred VS120 (Olympus, Hamburg, Germany).

Re-analysis of scRNA-seq Data. We re-analyzed single-cell transcriptomic data from bronchoalveolar lavage fluid (BAL) from patients with varying severity of COVID-19 disease and their respective healthy controls (Liao et al., 2020). The dataset is publicly available at https://covid19-balf.cells.ucsc.edu/. Downloaded data was imported into R environment version v3.6.3. Differential expression analysis was conducted using FindMarkers function in Seurat using the Wilcoxon test to compare mild and severe COVID-19 patients with healthy individuals for each cluster previously identified by authors. Differentially expressed genes between mild/severe COVID-19 patients and controls for each cluster were identified considering genes expressed in at least 5% of cells and FDR < 0.05 and |avg_logFC| > 0.1. In addition, a differentially expressed gene list comparing infected (identified SARS-Cov-2 transcripts) against non-infected alveolar macrophages were obtained from supplemental materials from (Ren et al., 2021). Gene Set Enrichment Analysis (GSEA) was performed using ClusterProfiler and fgsea R packages (Korotkevich et al., 2021; Wu et al., 2021) for each differentially expressed gene or log2 fold-change lists from Liao et al. (2020) and Ren et al. (2021) dataset. A custom gene set was also utilized as a reference for GSEA, incorporating GO:0006911, GO:0043277 gene

ontology terms, and additional efferocytic related genes from the literature (Penberthy and Ravichandran, 2016; Boada-Romero et al., 2020) (**Table S1**). Significantly enriched sets were identified considering terms with p-value < 0.05.

Data processing, quantification, and statistical analyses. Flow cytometric data processing was performed using FlowJo_V10 software (BD Biosciences). Images obtained by confocal and epifluorescence microscopy were analyzed using ImageJ (NIH). Data were plotted and analyzed with GraphPad Prism 8.4.2 software (GraphPad Prism Software Inc., San Diego, CA). The statistical tests used are listed in the legend of the figures. For the *in vitro* assays, we used Student's t-test to compare two experimental groups or one-way ANOVA, followed by ordinary ANOVA and multiple comparison correction, to compare three or more experimental groups. For the comparison between COVID-19 patients and healthy control datasets, normality tests were performed, and samples with non-Gaussian distribution were analyzed applying the Mann–Whitney test. For monocyte phenotyping from blood samples, the outliers were identified applying the ROUT method defining Q = 0.1% and then removed from the analyses. *p* values < 0.05 were considered significant.

Acknowledgements

The authors thank Denise M. da Fonseca, Elizabete R. Milani and Roberta R. C. Rosales (FMRP-USP) for technical assistance and Jennifer Martinez (NIEHS, NIH) for thoughtful insights and discussions.

Funding: This work was supported by grants from:

673 Fundação de Amparo a Pesquisa do Estado de São Paulo (FAPESP) grants
674 2018/25559-4 and 2020/05288-6 (L.D.C)
675 Coordenação de Aperfeiçoamento de Pessoal de Nível Superior (CAPES) grant
676 88887.507253/2020-00 (D. S. Z. and L.D.C.)
677 Conselho Nacional de Desenvolvimento Científico e Tecnológico (CNPq) grant
678 434538/2018-3 (L.D.C.)
679 D.S., A. C. G. S., T. S. R. are supported by FAPESP fellowships.

680

681 **Author Contributions**

682 Conceptualization: A. C. G. S., D. S., T. S. R., and L.D.C.
683 Methodology: A. C. G. S., D. S., T. S. R. and L.D.C
684 Investigation and data analysis: A. C. G. S., D. S., T. S. R.
685 Investigation and data analysis – specific experiments: M. F. R., E. G. F. F., D. L. A. T.,
686 M. H. F. L., D. B. C. N., and I. M. S. C.
687 Clinical data curation: N. B. A., M. C. G., L. P. B., M I. F. L., M. N. B., S. S. B., R. C. S.,
688 F. C. V., M. A. M., R. L. A., S. C. L. A, F. R. O., A. T. F., P. L. J. and R. D. R. O
689 Clinical data analysis: P. L. J. and R. D. R. O
690 Resources: C. M. S., J. E. T., A. B., S. O., D. B. C., L. A., A. Y. I , T. M. L., R. B. M., F.
691 V., E. A., T. M. C., J. C. A. F., A.T.F., H. I. N., D. S. Z., P. L. J. and R. D. R. O
692 Visualization: A.C.G.S., D. S. and I. C.
693 Funding acquisition and supervision: L. D. C.
694 Writing – original draft: D. S., A. C. G. S., T. S. R., and L. D. C
695 Writing – review and editing: all authors

Competing Interests

The authors declare no competing financial interests.

Data Availability

All data are available in the main text or supporting information.

References

A-Gonzalez N, Quintana JA, García-Silva S, Mazariegos M, Aleja AG de la, Nicolás-Ávila JAA, Walter W, Adrover JM, Crainiciuc G, Kuchroo VK, Rothlin CV, Peinado H, Castrillo A, Ricote M, Hidalgo A. 2017. Phagocytosis imprints heterogeneity in tissue-resident macrophages. *The Journal of experimental medicine* 214:1281–1296. doi:10.1084/jem.20161375

Banerjee S, Friggeri A, Liu G, Abraham E. 2010. The C-terminal acidic tail is responsible for the inhibitory effects of HMGB1 on efferocytosis. *J Leukocyte Biol* 88:973–979. doi:10.1189/jlb.0510262

Bastard P, Rosen LB, Zhang Q, Michailidis E, Hoffmann H-H, Zhang Y, Dorgham K, Philippot Q, Rosain J, Béziat V, Manry J, Shaw E, Haljasmägi L, Peterson P, Lorenzo L, Bizien L, Trouillet-Assant S, Dobbs K, Jesus AA de, Belot A, Kallaste A, Catherinot E, Tandjaoui-Lambiotte Y, Pen JL, Kerner G, Bigio B, Seeleuthner Y, Yang R, Bolze A, Spaan AN, Delmonte OM, Abers MS, Aiuti A, Casari G, Lampasona V, Piemonti L, Ciceri F, Bilguvar K, Lifton RP, Vasse M, Smadja DM, Migaud M, Hadjadj J, Terrier B, Duffy D, Quintana-Murci L, Beek D van de, Roussel L, Vinh DC, Tangye SG, Haerynck F, Dalmau D, Martinez-Picado J, Brodin P, Nussenzweig MC, Boisson-Dupuis S, Rodríguez-Gallego C, Vogt G, Mogensen TH, Oler AJ, Gu J, Burbelo PD, Cohen J, Biondi A, Bettini LR, D'Angio M, Bonfanti P, Rossignol P, Mayaux J, Rieux-Laucat F, Husebye ES, Fusco F, Ursini MV, Imberti L, Sottini A, Paghera S, Quiros-Roldan E, Rossi C, Castagnoli R, Montagna D, Licari A, Marseglia GL, Duval X, Ghosn J, Lab§ H, Group§ N-UIR to C, Clinicians§ C, Clinicians§ C-S, Group§ IC, Group§ FCCS, Consortium§ TMI, Cohort§ C-C, Biobank§ AUC-19, Effort§ CHG, Tsang JS, Goldbach-Mansky R, Kisand K, Lionakis MS, Puel A, Zhang S-Y, Holland SM, Gorochov G, Jouanguy E, Rice CM, Cobat A, Notarangelo LD, Abel L, Su HC, Casanova J-L. 2020. Auto-antibodies against type I IFNs in patients with life-threatening COVID-19. *Science* eabd4585. doi:10.1126/science.abd4585

Blanco-Melo D, Nilsson-Payant BE, Liu W-C, Uhl S, Hoagland D, Møller R, Jordan TX, Oishi K, Panis M, Sachs D, Wang TT, Schwartz RE, Lim JK, Albrecht RA, tenOever BR. 2020.

733 Imbalanced Host Response to SARS-CoV-2 Drives Development of COVID-19. *Cell*
734 181:1036-1045.e9. doi:10.1016/j.cell.2020.04.026
735 Boada-Romero E, Martinez J, Heckmann B, Green D. 2020. The clearance of dead cells by
736 efferocytosis. *Nat Rev Mol Cell Bio* 1–17. doi:10.1038/s41580-020-0232-1
737 Bosurgi L, Cao YG, Cabeza-Cabrerizo M, Tucci A, Hughes LD, Kong Y, Weinstein JS, Licona-
738 Limon P, Schmid ET, Pelorosso F, Gagliani N, Craft JE, Flavell RA, Ghosh S, Rothlin CV.
739 2017. Macrophage function in tissue repair and remodeling requires IL-4 or IL-13 with
740 apoptotic cells. *Sci New York N Y* 356:1072–1076. doi:10.1126/science.aai8132
741 Chan JF-W, Zhang AJ, Yuan S, Poon VK-M, Chan CC-S, Lee AC-Y, Chan W-M, Fan Z, Tsoi
742 H-W, Wen L, Liang R, Cao J, Chen Y, Tang K, Luo C, Cai J-P, Kok K-H, Chu H, Chan K-H,
743 Sridhar S, Chen Z, Chen H, To KK-W, Yuen K-Y. 2020. Simulation of the Clinical and
744 Pathological Manifestations of Coronavirus Disease 2019 (COVID-19) in a Golden Syrian
745 Hamster Model: Implications for Disease Pathogenesis and Transmissibility. *Clin Infect Dis*
746 *Official Publ Infect Dis Soc Am* 71:2428–2446. doi:10.1093/cid/ciaa325
747 Chen L, Long X, Xu Q, Tan J, Wang G, Cao Y, Wei J, Luo H, Zhu H, Huang Liang, Meng F,
748 Huang Lifang, Wang N, Zhou X, Zhao L, Chen X, Mao Z, Chen C, Li Z, Sun Z, Zhao J,
749 Wang D, Huang G, Wang W, Zhou J. 2020. Elevated serum levels of S100A8/A9 and
750 HMGB1 at hospital admission are correlated with inferior clinical outcomes in COVID-19
751 patients. *Cell Mol Immunol* 17:992–994. doi:10.1038/s41423-020-0492-x
752 Chu H, Chan JF-W, Yuen TT-T, Shuai H, Yuan S, Wang Y, Hu B, Yip CC-Y, Tsang JO-L,
753 Huang X, Chai Y, Yang D, Hou Y, Chik KK-H, Zhang X, Fung AY-F, Tsoi H-W, Cai J-P,
754 Chan W-M, Ip JD, Chu AW-H, Zhou J, Lung DC, Kok K-H, To KK-W, Tsang OT-Y, Chan
755 K-H, Yuen K-Y. 2020. Comparative tropism, replication kinetics, and cell damage profiling
756 of SARS-CoV-2 and SARS-CoV with implications for clinical manifestations,
757 transmissibility, and laboratory studies of COVID-19: an observational study. *Lancet Microbe*
758 1:e14–e23. doi:10.1016/s2666-5247(20)30004-5
759 Chu H, Shuai H, Hou Y, Zhang X, Wen L, Huang X, Hu B, Yang D, Wang Y, Yoon C, Wong
760 BH-Y, Li C, Zhao X, Poon VK-M, Cai J-P, Wong KK-Y, Yeung M-L, Zhou J, Au-Yeung
761 RK-H, Yuan S, Jin D-Y, Kok K-H, Perlman S, Chan JF-W, Yuen K-Y. 2021. Targeting
762 highly pathogenic coronavirus-induced apoptosis reduces viral pathogenesis and disease
763 severity. *Sci Adv* 7:eabf8577. doi:10.1126/sciadv.abf8577
764 Cohen PL, Caricchio R, Abraham V, Camenisch TD, Jennette JC, Roubey RAS, Earp HS,
765 Matsushima G, Reap EA. 2002. Delayed Apoptotic Cell Clearance and Lupus-like
766 Autoimmunity in Mice Lacking the c-mer Membrane Tyrosine Kinase. *J Exp Medicine*
767 196:135–140. doi:10.1084/jem.20012094
768 Corman VM, Landt O, Kaiser M, Molenkamp R, Meijer A, Chu DK, Bleicker T, Brünink S,
769 Schneider J, Schmidt ML, Mulders DG, Haagmans BL, Veer B van der, Brink S van den,
770 Wijsman L, Goderski G, Romette J-L, Ellis J, Zambon M, Peiris M, Goossens H, Reusken C,
771 Koopmans MP, Drosten C. 2020. Detection of 2019 novel coronavirus (2019-nCoV) by real-
772 time RT-PCR. *Eurosurveillance* 25:2000045. doi:10.2807/1560-7917.es.2020.25.3.2000045
773 Doran AC, Yurdagul A, Tabas I. 2020. Efferocytosis in health and disease. *Nat Rev Immunol*
774 20:254–267. doi:10.1038/s41577-019-0240-6
775 Fadok VA, Voelker DR, Campbell PA, Cohen JJ, Bratton DL, Henson PM. 1992. Exposure of
776 phosphatidylserine on the surface of apoptotic lymphocytes triggers specific recognition and
777 removal by macrophages. *J Immunol Baltim Md 1950* 148:2207–16.

778 Feng X, Deng T, Zhang Y, Su S, Wei C, Han D. 2011. Lipopolysaccharide inhibits macrophage
779 phagocytosis of apoptotic neutrophils by regulating the production of tumour necrosis factor α
780 and growth arrest-specific gene 6. *Immunology* 132:287–295. doi:10.1111/j.1365-
781 2567.2010.03364.x
782 Gomes R, Guerra-Sá R, Arruda E. 2009. Coxsackievirus B5 induced apoptosis of HeLa cells:
783 effects on p53 and SUMO. *Virology* 396:256–63. doi:10.1016/j.virol.2009.10.005
784 Hamers AAJ, Dinh HQ, Thomas GD, Marcovecchio P, Blatchley A, Nakao CS, Kim C,
785 McSkimming C, Taylor AM, Nguyen AT, McNamara CA, Hedrick CC. 2019. Human
786 Monocyte Heterogeneity as Revealed by High-Dimensional Mass Cytometry. *Arteriosclerosis*
787 *Thrombosis Vasc Biology* 39:25–36. doi:10.1161/atvbaha.118.311022
788 Han Y, Zhang H, Mu S, Wei W, Jin C, Xue Y, Tong C, Zha Y, Song Z, Gu G. 2020. Lactate
789 dehydrogenase, a Risk Factor of Severe COVID-19 Patients. *Medrxiv* 2020.03.24.20040162.
790 doi:10.1101/2020.03.24.20040162
791 Jamieson AM, Pasman L, Yu S, Gamradt P, Homer RJ, Decker T, Medzhitov R. 2013. Role of
792 Tissue Protection in Lethal Respiratory Viral-Bacterial Coinfection. *Science* 340:1230–1234.
793 doi:10.1126/science.1233632
794 Korotkevich G, Sukhov V, Budin N, Shpak B, Artyomov MN, Sergushichev A. 2021. Fast gene
795 set enrichment analysis. *Biorxiv* 060012. doi:10.1101/060012
796 Li Shaohua, Jiang L, Li X, Lin F, Wang Y, Li B, Jiang T, An W, Liu S, Liu H, Xu P, Zhao L,
797 Zhang L, Mu J, Wang H, Kang J, Li Y, Huang L, Zhu C, Zhao S, Lu J, Ji J, Zhao J. 2020.
798 Clinical and pathological investigation of patients with severe COVID-19. *Jci Insight* 5.
799 doi:10.1172/jci.insight.138070
800 Li Shufen, Zhang Y, Guan Z, Li H, Ye M, Chen X, Shen J, Zhou Y, Shi Z-L, Zhou P, Peng K.
801 2020. SARS-CoV-2 triggers inflammatory responses and cell death through caspase-8
802 activation. *Signal Transduct Target Ther* 5:235. doi:10.1038/s41392-020-00334-0
803 Liao M, Liu Y, Yuan J, Wen Y, Xu G, Zhao J, Cheng L, Li J, Wang X, Wang F, Liu L, Amit I,
804 Zhang S, Zhang Z. 2020. Single-cell landscape of bronchoalveolar immune cells in patients
805 with COVID-19. *Nat Med* 26:842–844. doi:10.1038/s41591-020-0901-9
806 Lucas C, Wong P, Klein J, Castro TBR, Silva J, Sundaram M, Ellingson MK, Mao T, Oh JE,
807 Israelow B, Takahashi T, Tokuyama M, Lu P, Venkataraman A, Park A, Mohanty S, Wang
808 H, Wyllie AL, Vogels CBF, Earnest R, Lapidus S, Ott IM, Moore AJ, Muenker MC, Fournier
809 JB, Campbell M, Odio CD, Casanovas-Massana A, Obaid A, Lu-Culligan A, Nelson A, Brito
810 A, Nunez A, Martin A, Watkins A, Geng B, Kalinich C, Harden C, Todeasa C, Jensen C, Kim
811 D, McDonald D, Shepard D, Courchaine E, White EB, Song E, Silva E, Kudo E, DeIuliis G,
812 Rahming H, Park H-J, Matos I, Nouws J, Valdez J, Fauver J, Lim J, Rose K-A, Anastasio K,
813 Brower K, Glick L, Sharma L, Sewanan L, Knaggs L, Minasyan M, Batsu M, Petrone M,
814 Kuang M, Nakahata M, Campbell M, Linehan M, Askenase MH, Simonov M, Smolgovsky
815 M, Sonnert N, Naushad N, Vijayakumar P, Martinello R, Datta R, Handoko R, Bermejo S,
816 Prophet S, Bickerton S, Velazquez S, Alpert T, Rice T, Khoury-Hanold W, Peng X, Yang Y,
817 Cao Y, Strong Y, Herbst R, Shaw AC, Medzhitov R, Schulz WL, Grubaugh ND, Cruz CD,
818 Farhadian S, Ko AI, Omer SB, Iwasaki A. 2020. Longitudinal analyses reveal immunological
819 misfiring in severe COVID-19. *Nature* 584:463–469. doi:10.1038/s41586-020-2588-y
820 Martins R, Carlos AR, Braza F, Thompson JA, Bastos-Amador P, Ramos S, Soares MP. 2019.
821 Disease Tolerance as an Inherent Component of Immunity. *Annu Rev Immunol* 37:405–437.
822 doi:10.1146/annurev-immunol-042718-041739

Michlewska S, Dransfield I, Megson IL, Rossi AG. 2008. Macrophage phagocytosis of apoptotic neutrophils is critically regulated by the opposing actions of pro-inflammatory and anti-inflammatory agents: key role for TNF-alpha. *Faseb J Official Publ Fed Am Soc Exp Biology* 23:844–54. doi:10.1096/fj.08-121228

Miyanishi M, Tada K, Koike M, Uchiyama Y, Kitamura T, Nagata S. 2007. Identification of Tim4 as a phosphatidylserine receptor. *Nature* 450:435–439. doi:10.1038/nature06307

Morioka S, Perry JSA, Raymond MH, Medina CB, Zhu Y, Zhao L, Serbulea V, Onengut-Gumuscu S, Leitinger N, Kucenas S, Rathmell JC, Makowski L, Ravichandran KS. 2018. Efferocytosis induces a novel SLC program to promote glucose uptake and lactate release. *Nature* 563:714–718. doi:10.1038/s41586-018-0735-5

Mulay A, Konda B, Garcia G, Yao C, Beil S, Villalba JM, Koziol C, Sen C, Purkayastha A, Kolls JayK, Pociask DA, Pessina P, Aja JS de, Garcia-de-Alba C, Kim CF, Gomperts B, Arumugaswami V, Stripp BR. 2021. SARS-CoV-2 infection of primary human lung epithelium for COVID-19 modeling and drug discovery. *Cell Reports* 35:109055. doi:10.1016/j.celrep.2021.109055

Murray PJ, Wynn TA. 2011. Protective and pathogenic functions of macrophage subsets. *Nat Rev Immunol* 11:723–737. doi:10.1038/nri3073

Mylvaganam S, Freeman SA, Grinstein S. 2021. The cytoskeleton in phagocytosis and macropinocytosis. *Curr Biol* 31:R619–R632. doi:10.1016/j.cub.2021.01.036

Nagata S. 2018. Apoptosis and Clearance of Apoptotic Cells. *Annu Rev Immunol* 36:489–517. doi:10.1146/annurev-immunol-042617-053010

Olagnier D, Lavergne R-A, Meunier E, Lefèvre L, Dardenne C, Aubouy A, Benoit-Vical F, Ryffel B, Coste A, Berry A, Pipy B. 2011. Nrf2, a PPARγ Alternative Pathway to Promote CD36 Expression on Inflammatory Macrophages: Implication for Malaria. *Plos Pathog* 7:e1002254. doi:10.1371/journal.ppat.1002254

Park D, Han CZ, Elliott MR, Kinchen JM, Trampont PC, Das S, Collins S, Lysiak JJ, Hoehn KL, Ravichandran KS. 2011. Continued clearance of apoptotic cells critically depends on the phagocyte Ucp2 protein. *Nature* 477:220–4. doi:10.1038/nature10340

Parks BW, Black LL, Zimmerman KA, Metz AE, Steele C, Murphy-Ullrich JE, Kabarowski JH. 2013. CD36, but not G2A, modulates efferocytosis, inflammation, and fibrosis following bleomycin-induced lung injury[S]. *J Lipid Res* 54:1114–1123. doi:10.1194/jlr.m035352

Penberthy KK, Ravichandran KS. 2016. Apoptotic cell recognition receptors and scavenger receptors. *Immunological reviews* 269:44–59. doi:10.1111/imr.12376

Peng Y, Elkon KB. 2011. Autoimmunity in MFG-E8–deficient mice is associated with altered trafficking and enhanced cross-presentation of apoptotic cell antigens. *J Clin Invest* 121:2221–2241. doi:10.1172/jci43254

Perry JSA, Morioka S, Medina CB, Etchegaray JI, Barron B, Raymond MH, Lucas CD, Onengut-Gumuscu S, Delpire E, Ravichandran KS. 2019. Interpreting an apoptotic corpse as anti-inflammatory involves a chloride sensing pathway. *Nat Cell Biol* 21:1532–1543. doi:10.1038/s41556-019-0431-1

Reed LJ, Muench H. 1938. A simple method of estimating fifty per cent endpoints. *Am J Epidemiol* 27:493–497. doi:10.1093/oxfordjournals.aje.a118408

Ren X, Wen W, Fan X, Hou W, Su Bin, Cai P, Li J, Liu Y, Tang F, Zhang F, Yang Y, He Jiangping, Ma W, He Jingjing, Wang P, Cao Q, Chen F, Chen Y, Cheng X, Deng G, Deng X, Ding W, Feng Y, Gan R, Guo C, Guo W, He S, Jiang C, Liang J, Li Y, Lin J, Ling Y, Liu H, Liu J, Liu N, Liu S-Q, Luo M, Ma Q, Song Q, Sun W, Wang G, Wang F, Wang Y, Wen X,

Wu Q, Xu G, Xie X, Xiong X, Xing X, Xu H, Yin C, Yu D, Yu K, Yuan J, Zhang B, Zhang P, Zhang T, Zhao J, Zhao Peidong, Zhou J, Zhou W, Zhong S, Zhong X, Zhang S, Zhu L, Zhu P, Zou B, Zou J, Zuo Z, Bai F, Huang X, Zhou P, Jiang Q, Huang Z, Bei J-X, Wei L, Bian X-W, Liu X, Cheng T, Li X, Zhao Pingsen, Wang F-S, Wang H, Su Bing, Zhang Zheng, Qu K, Wang X, Chen J, Jin R, Zhang Zemin. 2021. COVID-19 immune features revealed by a large-scale single-cell transcriptome atlas. *Cell* 184:1895-1913.e19. doi:10.1016/j.cell.2021.01.053

Ren Y, Shu T, Wu D, Mu J, Wang C, Huang M, Han Y, Zhang X-Y, Zhou W, Qiu Y, Zhou X. 2020. The ORF3a protein of SARS-CoV-2 induces apoptosis in cells. *Cell Mol Immunol* 17:881–883. doi:10.1038/s41423-020-0485-9

Rodrigues TS, Sá KSG de, Ishimoto AY, Becerra A, Oliveira S, Almeida L, Gonçalves AV, Perucello DB, Andrade WA, Castro R, Veras FP, Toller-Kawahisa JE, Nascimento DC, Lima MHF de, Silva CMS, Caetite DB, Martins RB, Castro IA, Pontelli MC, Barros FC de, Amaral NB do, Giannini MC, Bonjorno LP, Lopes MIF, Santana RC, Vilar FC, Auxiliadora-Martins M, Luppino-Assad R, Almeida SCL de, Oliveira FR de, Batah SS, Siyuan L, Benatti MN, Cunha TM, Alves-Filho JC, Cunha FQ, Cunha LD, Frantz FG, Kohlsdorf T, Fabro AT, Arruda E, Oliveira RDR de, Louzada-Junior P, Zamboni DS. 2020. Inflammasomes are activated in response to SARS-CoV-2 infection and are associated with COVID-19 severity in patients. *J Exp Med* 218. doi:10.1084/jem.20201707

Rodriguez-Manzanet R, Sanjuan MA, Wu HY, Quintana FJ, Xiao S, Anderson AC, Weiner HL, Green DR, Kuchroo VK. 2010. T and B cell hyperactivity and autoimmunity associated with niche-specific defects in apoptotic body clearance in TIM-4-deficient mice. *Proc National Acad Sci* 107:8706–8711. doi:10.1073/pnas.0910359107

Rothlin CV, Hille TD, Ghosh S. 2020. Determining the effector response to cell death. *Nat Rev Immunol* 1–13. doi:10.1038/s41577-020-00456-0

Satyanarayanan SK, Kebir DE, Soboh S, Butenko S, Sekheri M, Saadi J, Peled N, Assi S, Othman A, Schif-Zuck S, Feuermann Y, Barkan D, Sher N, Filep JG, Ariel A. 2019. IFN-β is a macrophage-derived effector cytokine facilitating the resolution of bacterial inflammation. *Nat Commun* 10:3471. doi:10.1038/s41467-019-10903-9

Schulte-Schrepping J, Reusch N, Paclik D, Baßler K, Schlickeiser S, Zhang B, Krämer B, Krammer T, Brumhard S, Bonaguro L, Domenico ED, Wendisch D, Grasshoff M, Kapellos TS, Beckstette M, Pecht T, Saglam A, Dietrich O, Mei HE, Schulz AR, Conrad C, Kunkel D, Vafadarnejad E, Xu C-J, Horne A, Herbert M, Drews A, Thibeault C, Pfeiffer M, Hippenstiel S, Hocke A, Müller-Redetzky H, Heim K-M, Machleidt F, Uhrig A, Jarcy LB de, Jürgens L, Stegemann M, Glösenkamp CR, Volk H-D, Goffinet C, Landthaler M, Wyler E, Georg P, Schneider M, Dang-Heine C, Neuwinger N, Kappert K, Tauber R, Corman V, Raabe J, Kaiser KM, Vinh MT, Rieke G, Meisel C, Ulas T, Becker M, Geffers R, Witzenrath M, Drosten C, Suttorp N, Kalle C von, Kurth F, Händler K, Schultze JL, Aschenbrenner AC, Li Y, Nattermann J, Sawitzki B, Saliba A-E, Sander LE, (DeCOI) DC-19 OI, Angelov A, Bals R, Bartholomäus A, Becker A, Bezdan D, Bonifacio E, Bork P, Clavel T, Colome-Tatche M, Diefenbach A, Dilthey A, Fischer N, Förstner K, Frick J-S, Gagneur J, Goesmann A, Hain T, Hummel M, Janssen S, Kalinowski J, Kallies R, Kehr B, Keller A, Kim-Hellmuth S, Klein C, Kohlbacher O, Korbel JO, Kurth I, Landthaler M, Li Y, Ludwig K, Makarewicz O, Marz M, McHardy A, Mertes C, Nöthen M, Nürnberg P, Ohler U, Ossowski S, Overmann J, Peter S, Pfeffer K, Poetsch AR, Pühler A, Rajewsky N, Ralser M, Rieß O, Ripke S, Rocha UN da, Rosenstiel P, Saliba A-E, Sander LE, Sawitzki B, Schiffer P, Schulte E-C, Schultze JL, Sczyrba A, Stegle O, Stoye J, Theis F, Vehreschild J, Vogel J, Kleist M von, Walker A,

915 Walter J, Wieczorek D, Ziebuhr J. 2020. Severe COVID-19 Is Marked by a Dysregulated
916 Myeloid Cell Compartment. *Cell* 182:1419-1440.e23. doi:10.1016/j.cell.2020.08.001
917 Siddiqi HK, Mehra MR. 2020. COVID-19 Illness in Native and Immunosuppressed States: A
918 Clinical-Therapeutic Staging Proposal. *J Hear Lung Transplant*.
919 doi:10.1016/j.healun.2020.03.012
920 Silvin A, Chapuis N, Dunsmore G, Goubet A-G, Dubuisson A, Derosa L, Almire C, Hénon C,
921 Kosmider O, Droin N, Rameau P, Catelain C, Alfaro A, Dussiau C, Friedrich C, Sourdeau E,
922 Marin N, Szwebel T-A, Cantin D, Mouthon L, Borderie D, Deloger M, Bredel D, Mouraud S,
923 Drubay D, Andrieu M, Lhonneur A-S, Saada V, Stoclin A, Willekens C, Pommeret F,
924 Griscelli F, Ng LG, Zhang Z, Bost P, Amit I, Barlesi F, Marabelle A, Pène F, Gachot B,
925 André F, Zitvogel L, Ginhoux F, Fontenay M, Solary E. 2020. Elevated Calprotectin and
926 Abnormal Myeloid Cell Subsets Discriminate Severe from Mild COVID-19. *Cell* 182:1401-
927 1418.e18. doi:10.1016/j.cell.2020.08.002
928 Tait JF, Smith C. 1999. Phosphatidylserine Receptors: Role of CD36 in Binding of Anionic
929 Phospholipid Vesicles to Monocytic Cells*. *J Biol Chem* 274:3048–3054.
930 doi:10.1074/jbc.274.5.3048
931 Thorp E, Vaisar T, Subramanian M, Mautner L, Blobel C, Tabas I. 2011. Shedding of the Mer
932 Tyrosine Kinase Receptor Is Mediated by ADAM17 Protein through a Pathway Involving
933 Reactive Oxygen Species, Protein Kinase Cδ, and p38 Mitogen-activated Protein Kinase
934 (MAPK). *J Biol Chem* 286:33335–33344. doi:10.1074/jbc.m111.263020
935 Valle DMD, Kim-Schulze S, Huang H-H, Beckmann ND, Nirenberg S, Wang B, Lavin Y,
936 Swartz TH, Madduri D, Stock A, Marron TU, Xie H, Patel M, Tuballes K, Oekelen OV,
937 Rahman A, Kovatch P, Aberg JA, Schadt E, Jagannath S, Mazumdar M, Charney AW, Firpo-
938 Betancourt A, Mendu DR, Jhang J, Reich D, Sigel K, Cordon-Cardo C, Feldmann M, Parekh
939 S, Merad M, Gnjatic S. 2020. An inflammatory cytokine signature predicts COVID-19
940 severity and survival. *Nat Med* 26:1636–1643. doi:10.1038/s41591-020-1051-9
941 Veras FP, Pontelli MC, Silva CM, Toller-Kawahisa JE, Lima M de, Nascimento DC, Schneider
942 AH, Caetité D, Tavares LA, Paiva IM, Rosales R, Colón D, Martins R, Castro IA, Almeida
943 GM, Lopes MIF, Benatti MN, Bonjorno LP, Giannini MC, Luppino-Assad R, Almeida SL,
944 Vilar F, Santana R, Bollela VR, Auxiliadora-Martins M, Borges M, Miranda CH, Pazin-Filho
945 A, Silva LLP da, Cunha L, Zamboni DS, Dal-Pizzol F, Leiria LO, Siyuan L, Batah S, Fabro
946 A, Mauad T, Dolhnikoff M, Duarte-Neto A, Saldiva P, Cunha TM, Alves-Filho JC, Arruda E,
947 Louzada-Junior P, Oliveira RD, Cunha FQ. 2020. SARS-CoV-2–triggered neutrophil
948 extracellular traps mediate COVID-19 pathology. *J Exp Med* 217. doi:10.1084/jem.20201129
949 Wang Y, Subramanian M, Yurdagul A, Barbosa-Lorenzi VC, Cai B, Juan-Sanz J de, Ryan TA,
950 Nomura M, Maxfield FR, Tabas I. 2017. Mitochondrial Fission Promotes the Continued
951 Clearance of Apoptotic Cells by Macrophages. *Cell* 171:331-345.e22.
952 doi:10.1016/j.cell.2017.08.041
953 Webb BJ, Peltan ID, Jensen P, Hoda D, Hunter B, Silver A, Starr N, Buckel W, Grisel N,
954 Hummel E, Snow G, Morris D, Stenehjem E, Srivastava R, Brown SM. 2020. Clinical criteria
955 for COVID-19-associated hyperinflammatory syndrome: a cohort study. *Lancet*
956 *Rheumatology*. doi:10.1016/s2665-9913(20)30343-x
957 Wu T, Hu E, Xu S, Chen M, Guo P, Dai Z, Feng T, Zhou L, Tang W, Zhan L, Fu X, Liu S, Bo
958 X, Yu G. 2021. clusterProfiler 4.0: A universal enrichment tool for interpreting omics data.
959 *Innovation* 2:100141. doi:10.1016/j.xinn.2021.100141

Yurdagul A, Subramanian M, Wang X, Crown SB, Ilkayeva OR, Darville L, Kolluru GK, Rymond CC, Gerlach BD, Zheng Z, Kuriakose G, Kevil CG, Koomen JM, Cleveland JL, Muoio DM, Tabas I. 2020. Macrophage Metabolism of Apoptotic Cell-Derived Arginine Promotes Continual Efferocytosis and Resolution of Injury. *Cell Metab* 31:518-533.e10. doi:10.1016/j.cmet.2020.01.001

Zhu N, Wang Wenling, Liu Z, Liang C, Wang Wen, Ye F, Huang B, Zhao L, Wang H, Zhou W, Deng Y, Mao L, Su C, Qiang G, Jiang T, Zhao J, Wu G, Song J, Tan W. 2020. Morphogenesis and cytopathic effect of SARS-CoV-2 infection in human airway epithelial cells. *Nat Commun* 11:3910. doi:10.1038/s41467-020-17796-z

Zuniga M, Gomes C, Carsons SE, Bender MT, Cotzia P, Miao QR, Lee DC, Rodriguez A. 2021. Autoimmunity to Annexin A2 predicts mortality among hospitalised COVID-19 patients. *Eur Respir J* 2100918. doi:10.1183/13993003.00918-2021

Zuo Y, Estes SK, Ali RA, Gandhi AA, Yalavarthi S, Shi H, Sule G, Gockman K, Madison JA, Zuo M, Yadav V, Wang J, Woodard W, Lezak SP, Lugogo NL, Smith SA, Morrissey JH, Kanthi Y, Knight JS. 2020. Prothrombotic autoantibodies in serum from patients hospitalized with COVID-19. *Sci Transl Med* 12:eabd3876. doi:10.1126/scitranslmed.abd3876

Figure captions

Figure 1. Macrophages engulf apoptotic cells carrying viable SARS-CoV-2

(A-B) Representative histological findings in post-mortem lung tissue from COVID-19 patients, obtained by ultrasound-guided minimally invasive autopsy. **(A)** Representative differential interference contrast (upper panel) and immunofluorescence (middle panel) images of tissue from P1 patient, immunolabelled with anti-cleaved caspase 3 (red), anti-dsRNA (SARS-CoV2, green), and stained with DAPI (nuclei, blue) for the detection of caspase-3 activation in infected cells. The bottom panels show higher magnification of the two selected areas. Arrows indicate cells positive for both Cl-caspase-3 and dsRNA (purple arrows: ciliated pseudostratified epithelia of a respiratory bronchiole; white arrows: type II pneumocytes; white arrowheads: type I pneumocytes; *cleaved-Casp3^{+} non-epithelial cell). Tissues were scanned by wide-field epifluorescence imaging. Scale bar: 50 µm. **(B)** Representative immunofluorescence image of tissue from P1 patient immunolabelled for the detection of efferocytosis in situ with anti-CD68 (detecting

macrophages, white), anti-cytokeratin18 (detecting epithelial cells, red), anti-Spike (detecting SARS-CoV-2, green), and stained with Hoescht (nuclei, blue). Bottom panels show higher magnification of (a) $CD68^+$ $Spike^+$ macrophage; (b) $CD68^+$ macrophage with $cytokeratin18^+$ content and Spike labeling in the cytosol. Yellow arrows: $cytokeratin18^+$ cells; Yellow arrowheads: $CD68^+$ cells. Tissues were scanned by wide-field epifluorescence imaging. Scale bar: 50 µm; scale bar for inset: 10 µm.

(C) PtdSer exposure on the surface of Calu-3 and Vero CCL81 cells in response to UV irradiation or infection with SARS-CoV-2 (Cov2) for 48h, assessed by annexin V binding (percentage of annexin V^+ cells) and flow cytometric analysis. The gating strategy is shown in Figure S1B.

(D) Flow cytometric analysis of caspase-3 cleavage (Cl-caspase-3) in Calu-3 cells unstimulated (Cntrl) or infected with SARS-CoV-2 (CoV2) for 48h. The pan-caspase inhibitor z-VAD-FMK (zVAD; 20 µM) or vehicle (DMSO) were added to cell cultures after viral adsorption. Representative histogram, geometric mean fluorescence intensity (MFI), and frequency of Cl-caspase-3^+ cells (gated on Total cells/Single cells) are shown. The black line on the histogram represents the control sample labeled with secondary antibody only.

(E) Quantification by $TCID_{50}$ of SARS-CoV-2 viral loads in Vero CCL81 infected cells. Cells were collected 48h post-infection, and viral loads were estimated for normalized amounts (10^6 cells) of pre-sorted (Total cells) or Annexin V^+ (Ann^+ cells) and Annexin V^- (Ann^- cells) cells isolated by magnetic separation.

(F) Uptake of apoptotic Vero CCL81 cells (labeled with CTFR) in response to UV irradiation (UV-AC) or infection with SARS-CoV-2 for 48h (Cov2-AC) by human monocyte-derived macrophages (labeled with CTV). Macrophages were co-incubated with AC for 2h, and

internalization was assessed by flow cytometry. Representative plot and percentage of engulfment (gated on Total cells/Single cells/Live cells/CTV^+ cells; gating strategy in Figure S1D) are shown. **(G)** Representative maximal projection of scanning confocal images showing the uptake of UV-AC or CoV2-AC (from Vero CCL81 cells, CFSE-labelled, green) by human monocyte-derived macrophages after 2h of co-incubation. Samples were stained with Hoescht (nuclei, blue) and were immunolabelled with anti-Spike (SARS-CoV-2, red) and anti-CD11b (macrophage, white). Scale bar: 5 μm.

Boxes represent the mean of three (C, E) or five (D, F) biological replicates, and error bars are ± S.E.M. Each biological replicate is shown as a circle. Significance was calculated by Student's test (C) or ANOVA (D, E). *, $p<0.05$ comparing the indicated groups; ns: non-significant. Data shown are from one representative out of two experiments performed independently with similar results.

Figure. 2. Engulfment of SARS-CoV-2-infected dying cells impairs macrophage anti-inflammatory functions.

Macrophages were unstimulated (Cntrl), co-incubated with apoptotic Vero CCL81 cells (AC) isolated from UV-irradiated (UV-AC) or SARS-CoV-2-infected (CoV2-AC) cultures, stimulated with the supernatants of infected apoptotic cells (CoV2-AC Sup), or infected with CoV2 at MOI of 1 (CoV2), as indicated.

(A) Heatmap showing the expression of M2-marker genes (*CCL18*, *MRC1*, *MMP9*, *PPARγ,* and *CD163*) in human monocyte-derived macrophages 24h after stimulation, calculated as log2 fold change relative to Cntrl. mRNA expression was determined by RT-qPCR and normalized to *GAPDH*. Data represent the mean of biological triplicates.

(B) Flow cytometric analysis of CD206 expression on the cell surface of human monocyte-derived macrophages (gated on Total cells/Single cells/Live cells; gating strategy in Figure S2A) 24h after stimulation. Representative histograms and quantification of geometric mean fluorescence intensity (MFI) are shown. The black line on the histogram represents FMO control.

(C-D) Flow cytometric analysis of CD206 expression on the cell surface of THP1-derived macrophages 24h after stimulation. **(C)** Where indicated, isolated CoV2-AC were UV-irradiated for 20 min prior to co-incubation to inactivate SARS-CoV-2. Quantification of CD206 MFI is shown. **(D)** The responses of macrophages to sterile UV-AC and virus-loaded CoV2-AC were compared to infection with CoV2 in the presence of UV-AC (UV-AC + CoV2). Quantification of CD206 MFI is shown.

(E) *IL6* expression in monocyte-derived macrophages 24h after stimulation showed as fold change relative to Cntrl. mRNA expression was determined by RT-qPCR and normalized to GAPDH.

(F) CBA quantification of IL-6 and IL-1β in the culture supernatants of the monocyte-derived macrophages 24h after stimulation.

(G) ELISA quantification of IL-6 in the culture supernatants of THP1-derived macrophages 24h after stimulation. Where indicated, isolated CoV2-AC were UV-irradiated (UV) for 20min or fixed with 2% paraformaldehyde (Fix) for 10 min prior to co-incubation.

(H-J) ELISA quantification of IL-6 in the culture supernatants of human monocyte-derived macrophages 24h after stimulation. **(H)** IL-6 secretion in response to CoV2-AC was compared to apoptotic cells isolated from Vero CCL81 cells similarly infected with Coxsackievirus (Coxsackie-AC). **(I)** PtdSer on the surface of CoV2-AC was blocked by incubation with Annexin V (Ann, 0.1 μg/mL) prior to addition to macrophage cultures (supplemented with Ca^{+2}) to inhibit AC binding.

(J) CoV2-AC and macrophages were co-incubated in the presence of Cytochalasin D (Cyto D, 10 μM) to inhibit AC internalization.

Boxes represent the mean of three biological replicates using cells from a single donor (B, E, F, I, and J), two donors (H), or THP-1-derived cells (C, G, H). Error bars are ± S.E.M. Each biological replicate is shown as a circle. Significance was calculated by ANOVA. *, $p<0.05$ comparing the indicated groups; ns: non-significant. Data shown are from one representative out of at least two experiments performed independently with similar results.

Figure 3. Engulfment of SARS-CoV-2-infected dying cells suppresses continual efferocytosis by macrophages

(**A**) Expression of efferocytic receptors in human monocyte-derived macrophages. Macrophages were unstimulated (Cntrl), co-incubated for 24h with apoptotic Vero CCL81 cells (AC) isolated from UV-irradiated (UV-AC) or SARS-CoV-2-infected (CoV2-AC) cultures, or infected with CoV2 at MOI of 1 (CoV2), as indicated. Expression of *CD36*, *SRA-I*, *ITGB5*, *TIMD4*, and *MERTK* are showed as fold change relative to Cntrl. mRNA levels were determined by RT-qPCR and normalized to *GAPDH*.

(B-D) Flow cytometric analysis of two-step efferocytosis *in vitro*. **(B)** Schematic representation of consecutive co-incubations of THP1-derived macrophages with apoptotic cells prior to the assessment of cell corpse uptake by flow cytometry. **(C)** Percentage of macrophages (CTV-labelled) with internalized UV-AC or CoV2-AC isolated from Vero CCL81 cell cultures (labeled with pHRodo), 18h after co-incubation. $pHRodo^+$ macrophages were gated on Total cells/Single cells/Live cells/CTV^+ (gating strategy is displayed in Figure S2L). **(D)** Macrophages were subsequently incubated with CTFR-labelled, UV-irradiated apoptotic Jurkat cells (UV-Jurkat) for

2h. UV-Jurkat uptake in 2nd round of engulfment is shown as the percentage of CTFR+ macrophages within PhRodo+ populations (gated on Total cells/Single cells/Live cells/ CTV+/ pHRodo+).

Boxes represent the mean of three biological replicates using cells from a single donor in (A) or THP-1-derived macrophages in quadruplicate (C and D). Error bars are ± S.E.M. Each biological replicate is shown as a circle. Significance was calculated by ANOVA (A) or Student's test (C and D). *, $p<0.05$ comparing the indicated groups; ns: non-significant. Data shown are from one representative out of two experiments performed independently with similar results.

Figures 4. Lung monocytes and macrophages of severe COVID-19 patients express reduced levels of efferocytic receptors.

(A-B) Representative histological findings in post-mortem lung tissue from control tissue (Cntrl) and COVID-19 patients, obtained by ultrasound-guided minimally invasive autopsy. Tissue samples were immunolabelled with anti-S100A9 (phagocytes, green), **(A)** anti-CD36 (red), or **(B)** anti-MERTK (red) and stained with DAPI (nuclei, blue). Representative images show cropped details of lung tissues scanned by wide-field epifluorescence imaging. Scale bar: 10 µm. The mean fluorescence intensity (MFI) of CD36 and MERTK of at least 200 S1009+ cells are shown (n = 3 individuals per group).

(C) GSEA analysis for efferocytosis-related gene sets in early-infiltrating phagocytes (S1009+ CCL18-) and in anti-inflammatory monocytes-derived macrophages (CD14+ S11009- CCL18+) clusters from the bronchoalveolar lavage of mild (M) and severe (S) COVID-19 patients versus healthy individuals. The corrplot depicts the normalized enrichment score (NES), and p value for the gene sets indicated on the y axis.

(D) Enriched efferocytosis-related Gene Ontology (GO) terms in genes repressed in virus-positive alveolar macrophages versus virus-negative cells.

(E) mRNA expression of efferocytic receptors *CD36*, *SRA-I*, *ITGB5*, *TIMD4*, and *MERTK* in PMBC isolated from the blood of healthy donors (HC, n=25) or patients with COVID-19 (n=42). mRNA levels were determined by RT-qPCR and normalized to *GAPDH*.

(F) mRNA expression of efferocytic receptors *CD36*, *SRA-I*, *ITGB5*, *TIMD4*, and *MERTK* in PMBC isolated from the blood of healthy donors (HC, n=13) or patients with acute respiratory distress syndrome unrelated to COVID-19 (non-COVID-19 ARDS, n=13). mRNA levels were determined by RT-qPCR and normalized to *GAPDH*.

(G) Stratification of *CD36*, *SRA-1*, and *TIMD4* expression according to COVID-19 patients' hyperinflammation score (cHIS) (n=42).

(H) Representative maximal projection of scanning confocal images showing the uptake of AC by monocytes from healthy donors (HC, n=25) and COVID-19 patients (n=16) after 2h of co-incubation. Actin filaments (F-actin) were stained with phalloidin (AF-488, green), and the nuclei were stained with Hoescht (blue). White arrows indicate transient reorganization of actin filament upon engulfment. Scale bar: 5 µm. The uptake of AC by the monocytes was assessed and associated with the cHIS score of the patients.

Dots represent an $S1009^{+}$ cell (A and B) or data from each donor (E-H), the crossing line represents the mean, and error bars are ± S.E.M. Significance was calculated by Mann-Whitney test (A and B, E-F) or ANOVA (G and H). *, $p<0.05$ comparing the indicated groups; ns: non-significant.

Supporting information captions

Figure S1. SARS-CoV-2 -apoptotic cells are engulfed by macrophages

(A) Representative histological findings in post-mortem lung tissue from COVID-19 patients, obtained by ultrasound-guided minimally invasive autopsy. Representative differential interference contrast (upper panel) and immunofluorescence (middle panel) images of tissue from P2 patient immunolabelled with anti-cleaved caspase 3 (red), anti-dsRNA (SARS-CoV2, green), and stained with DAPI (nuclei, blue) for the detection of caspase-3 activation in infected cells. The bottom panels show higher magnification of the three selected areas. Arrows indicate cells positive for both Cl-caspase-3 and dsRNA (white arrows: type II pneumocytes; white arrowheads: type I pneumocytes; *cleaved-Casp3^{+} non-epithelial cell). Tissues were scanned by wide-field epifluorescence imaging. Scale bar: 100 µm (upper and middle panels) or 50 µm (selected areas).

(B) Representative gating strategy used to determine the PtdSer exposure on the surface of Calu-3 and Vero CCL81 cells in response to UV irradiation or infection with SARS-CoV-2 (Cov2) for 48h, assessed by annexin V binding and flow cytometric analysis (related to Figure 1C)

(C) $TCID_{50}$ quantification of SARS-CoV-2 viral loads from detached, apoptotic Calu-3 and Vero CCL81 cells (CoV2-AC, 10^6 cells) and their cell-free supernatants, collected 48h post-infection and isolated as described in the Methods.

(D) Uptake of apoptotic Calu-3 and Vero CCL81 cells (labeled with CFSE) in response to UV irradiation (UV-AC) or infection with SARS-CoV-2 for 48h (Cov2-AC) by THP-1-derived macrophages (labeled with CTFR). Macrophages were co-incubated with AC for 2h, and internalization was assessed by flow cytometry. Representative gating strategy, plots, and percentage of engulfment (gated on Total cells/Single cells/Live cells/CTFR^{+} cells) are shown.

(E) Human monocyte-derived macrophages or THP-1-derived macrophages were unstimulated (Cntrl), co-incubated with apoptotic Vero CCL81 cells isolated from UV-irradiated (UV-AC) or SARS-CoV-2-infected (CoV2-AC) cultures, stimulated with the supernatants of infected apoptotic cells (CoV2-AC Sup), or infected with SARS-CoV-2 at MOI of 1 (CoV2), as indicated. The percentage of cellular viability was measured using a viability probe 24h post-stimulation and analysis by flow cytometry (gated on Total cells/Single cells).

Boxes represent the mean of three biological replicates, and error bars are ± S.E.M. Each biological replicate is shown as a circle. Significance was calculated by Student's test (C-D) or ANOVA (E). *, $p<0.05$ comparing the indicated groups; ns: non-significant. Data shown are from one representative out of two experiments performed independently with similar results.

Figure S2. Engulfment of SARS-CoV-2-infected dying cells switches macrophage phenotype in response to efferocytosis.

(A) Representative gating strategy used to determine the CD206 expression on the surface of macrophages in response to the different stimulus by flow cytometry (backgating corresponds to FMO control showed in Fig. 2B)

(B) THP-1-derived macrophages were unstimulated (Cntrl), co-incubated with UV-AC, CoV2-AC, or CoV2-AC Sup obtained from Vero CCL81 cells, or infected with CoV2, as indicated. Expression of *MRC1* in macrophages showed as fold change relative to Cntrl was assessed 24h after stimulation. mRNA expression was determined by RT-qPCR and normalized to *GAPDH*.

(C-D) THP-1-derived macrophages were incubated with UV-AC, Cov2-C, or CoV2-Sup obtained from Calu-3 **(C)** or Vero CCL81 **(D)** infected cell cultures. CD206 expression on the cell surface 24h after stimulation was assessed by flow cytometry (gated on Total cells/Single cells/Live cells).

Representative histograms and quantification of geometric mean fluorescence intensity (MFI) of CD206 are shown.

(E) Quantification by $TCID_{50}$ of the SARS-CoV-2 viral loads in 10^6 AC isolated from Vero CCL81 infected cells, either intact (CoV2-AC) or UV-irradiated for 20 min for viral inactivation (CoV2-AC UV).

(F) THP-1-derived macrophages were incubated with UV-AC, Cov2-AC, or CoV2-Sup obtained from infected Vero CCL81 cells or infected with Cov2. Expression of *MRC1* in macrophages showed as fold change relative to Cntrl was assessed 24h after stimulation. mRNA expression was determined by RT-qPCR and normalized to *GAPDH*.

(G-H) THP-1-derived macrophages were incubated for 24h with UV-AC, Cov2-C, or CoV2-Sup obtained from Calu-3 or Vero CCL81 infected cell cultures, as indicated. IL-6 **(G)** and IL-1β **(H)** in the culture supernatants were quantified by CBA.

(I) Quantification by $TCID_{50}$ of the viral loads in 10^6 AC isolated from Vero CCL81 cells similarly infected with either Coxsackie virus (Coxsackie-AC) or SARS-CoV-2 (CoV2-AC).

(J) ELISA quantification of IL-6 in the culture supernatants of THP-1-derived macrophages stimulated with Cov2-AC for 24h. PtdSer on the cell surface was blocked to inhibit AC binding by incubation of CoV2-AC with Annexin V (Ann, 0.01 and 0.1 µg/mL) prior to addition to macrophage cultures.

(K) THP-1-derived macrophages were incubated with UV-AC or Cov2-AC obtained from infected Vero CCL81 cells or infected with CoV2. Expression of the efferocytic receptors *CD36*, *SRA-I*, *ITGB5*, *TIMD4*, and *MERTK* showed as fold change relative to Cntrl was assessed 24h after stimulation. mRNA levels were determined by RT-qPCR and normalized to *GAPDH*.

(L) Representative gating strategy used to determine CTV-labelled macrophage populations for the two-step efferocytosis experiment showed in Figures 3C and D.

(M) THP-1-derived macrophages (CTV-labelled) were infected or not with SARS-CoV-2 (CoV2) at MOI of 1 for 18h and subsequently were incubated with CTFR-labelled, UV-irradiated apoptotic Jurkat cells (UV-Jurkat) for 2h. UV-Jurkat uptake is shown as the percentage of $CTFR^+$ (gated on Total cells/Single cells/Live cells/ CTV^+).

Boxes represent the mean of three biological replicates, and error bars are ± S.E.M. Each biological replicate is shown as a circle. Significance was calculated by ANOVA (B-D, F-H, and J-K) or Student's test (I and M). *, $p<0.05$ comparing the indicated groups; ns: non-significant. Data shown are from one representative out of two experiments performed independently with similar results.

Figure S3. Analysis of cytokine production and monocyte subpopulations in COVID-19 patients.

(A) CBA quantification of IL-6, IL-8, IL-10, IL-1β, TNF-α, and IL-12 in the plasma from healthy donors (HC, n=19) and COVID-19 patients (n=28).

(B) Representative gating strategy used to determine the percentage of classical, intermediate, non-classical monocyte subpopulations, CD36, and HLA-DR expression on the surface of blood monocytes from HC and COVID-19 patients (related to Figs. S3 C-I). Displayed plots correspond to CD36-PE FMO control.

(C-D) The frequency **(C)** and absolute number **(D)** of $CD14^+$ blood monocytes from HC (n=22) and COVID-19 patients (n=26) were determined by flow cytometry (gated on Total cells/Single cells/Live cells/Lin^-).

(E) Percentage of HLA-DR^{+} monocytes in blood from healthy donors (HC, n=22) and COVID-19 patients (n=26), determined by flow cytometry (gated on Total cells/Single cells/Live cells/Lin^{-} /CD14^{+}).

(F-H) Frequency of **(F)** classical CD14^{+}CD16^{-}, **(G)** intermediate CD14^{hi}CD16^{+} and **(H)** non-classical CD14^{int}CD16^{+} monocytes in blood samples from healthy donors (HC, n=22) and COVID-19 patients (n=26) are shown (gated on Total cells/Single cells/Live cells/Lin^{-} CD14^{+}).

(I) Representative plots, frequency, and MFI of CD36 expression in CD14^{hi} monocytes from HC and COVID-19 patients (gated on Total cells/Single cells/Live cells/Lin^{-} CD14^{hi}).

(J) The uptake of zymosan particles (labeled with Texas-Red) by monocytes from healthy donors (HC, n=7) and COVID-19 patients (n=7) was determined by epifluorescence microscopy. Each dot represents the data from each donor, the crossing line represents mean, and error bars ± S.E.M. Significance was calculated by the Mann-Whitney test (A and C-I) or Student's test (J). *, $p<0.05$ comparing the indicated groups; ns: non-significant.

Table S1. Custom gene sets incorporating associated to efferocytic pathway and related to human diseases (related to Figure 4C).

Table S2. Medical characteristics of COVID-19 patients.

Table S3. Medical characteristics of nonCOVID-19 ARDS patients.

Figure 1 **Salina, dos-Santos, Rodrigues *et al.***

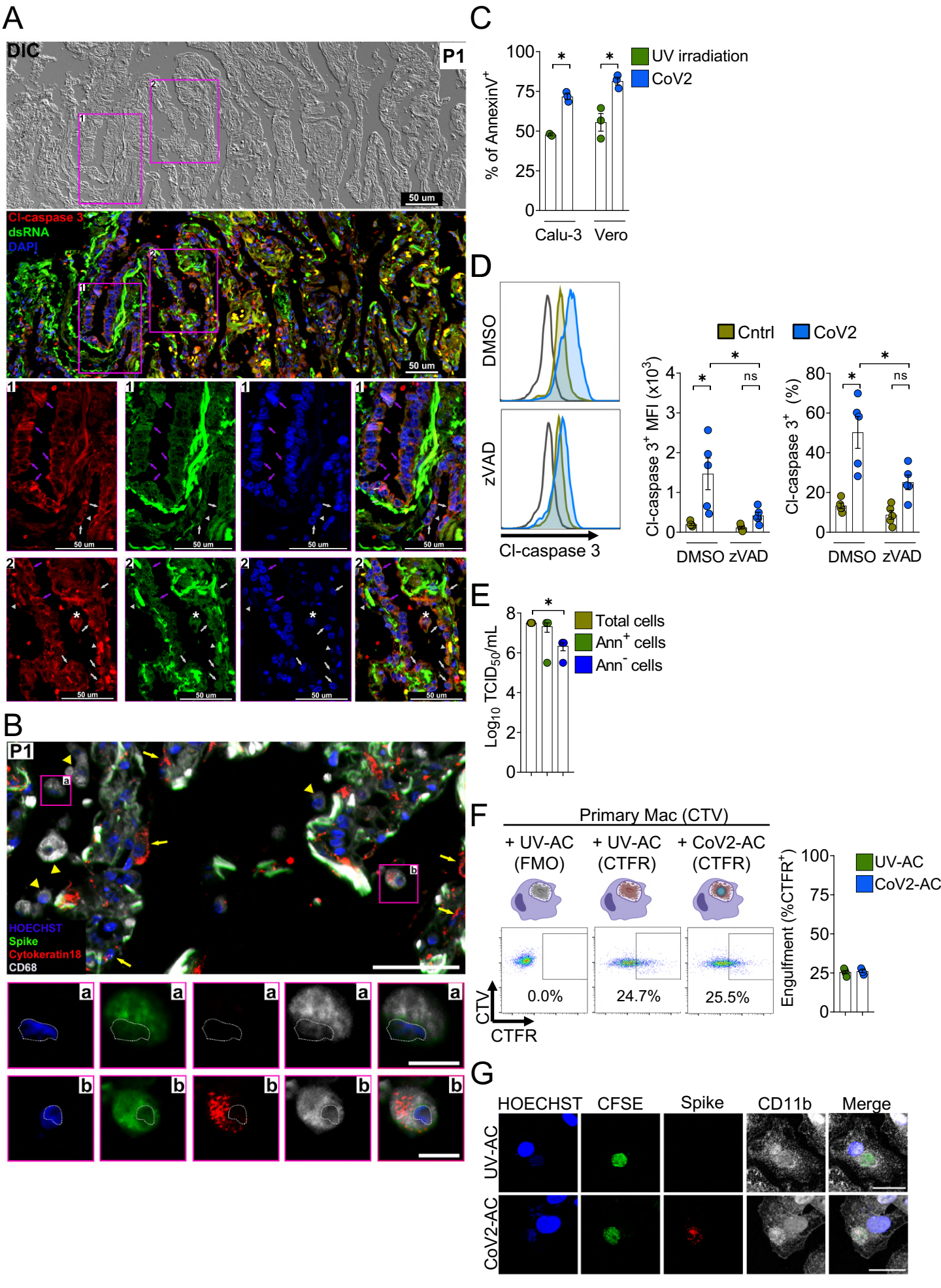

Figure 2

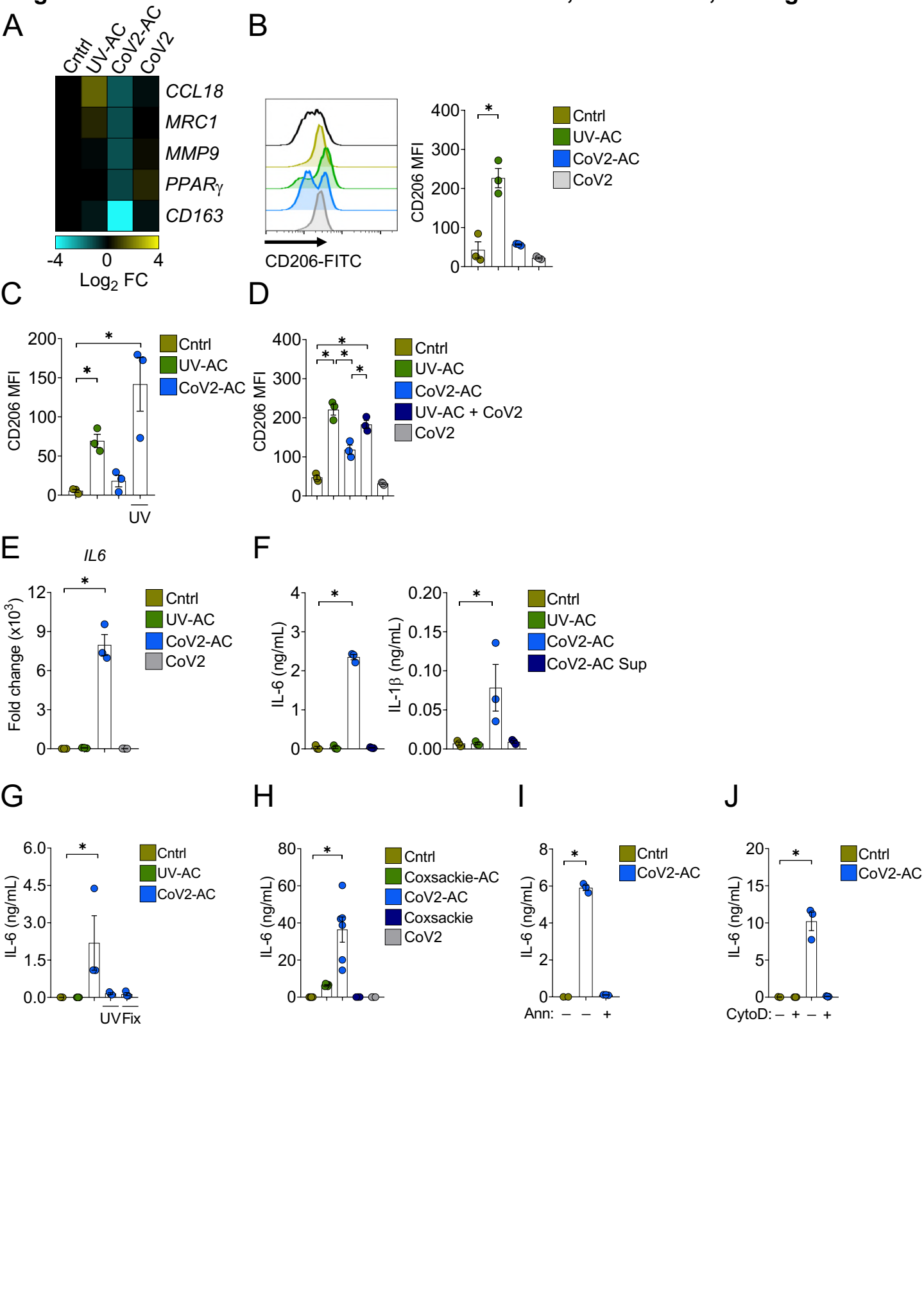

Figure 3

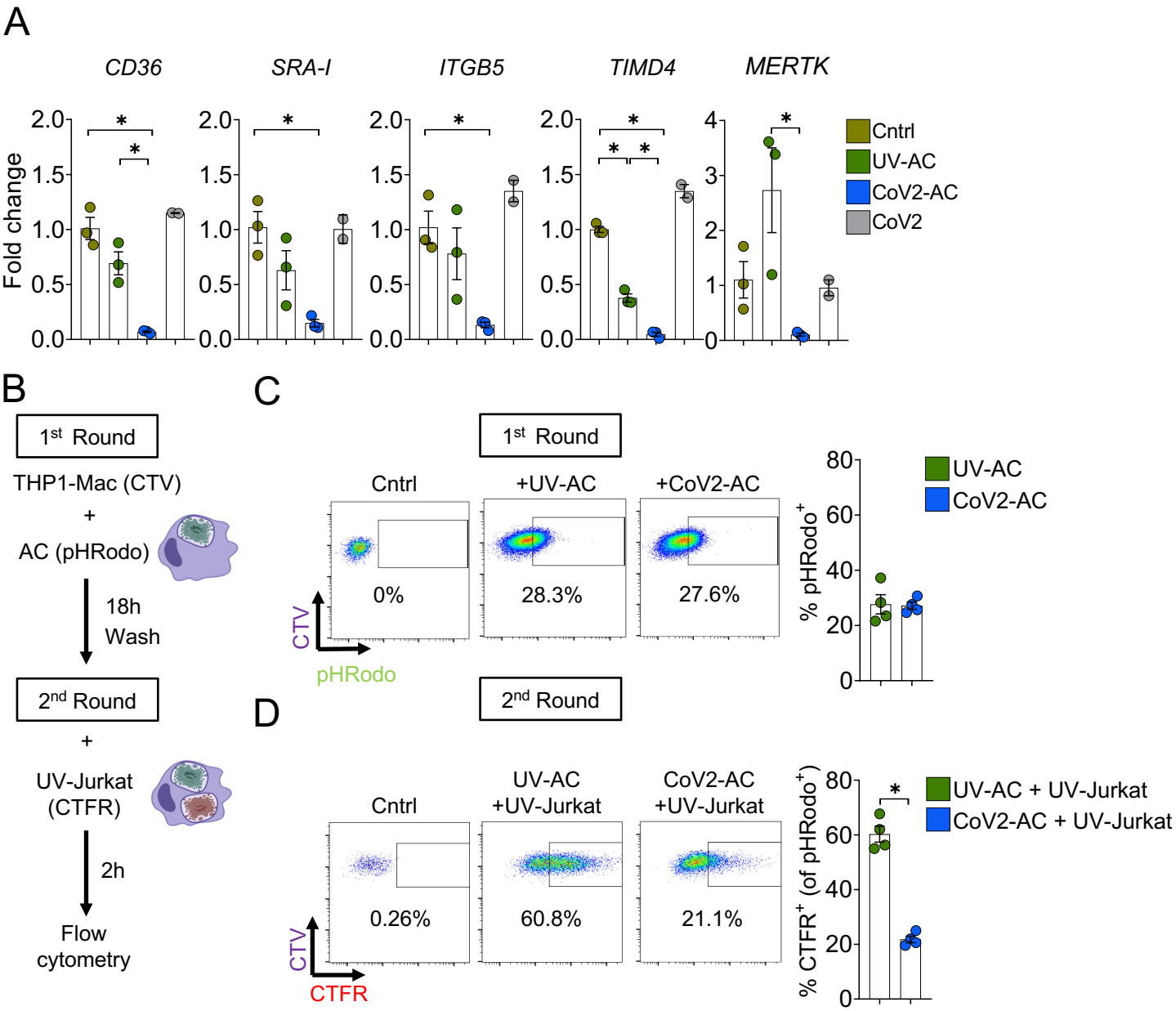

Figure 4

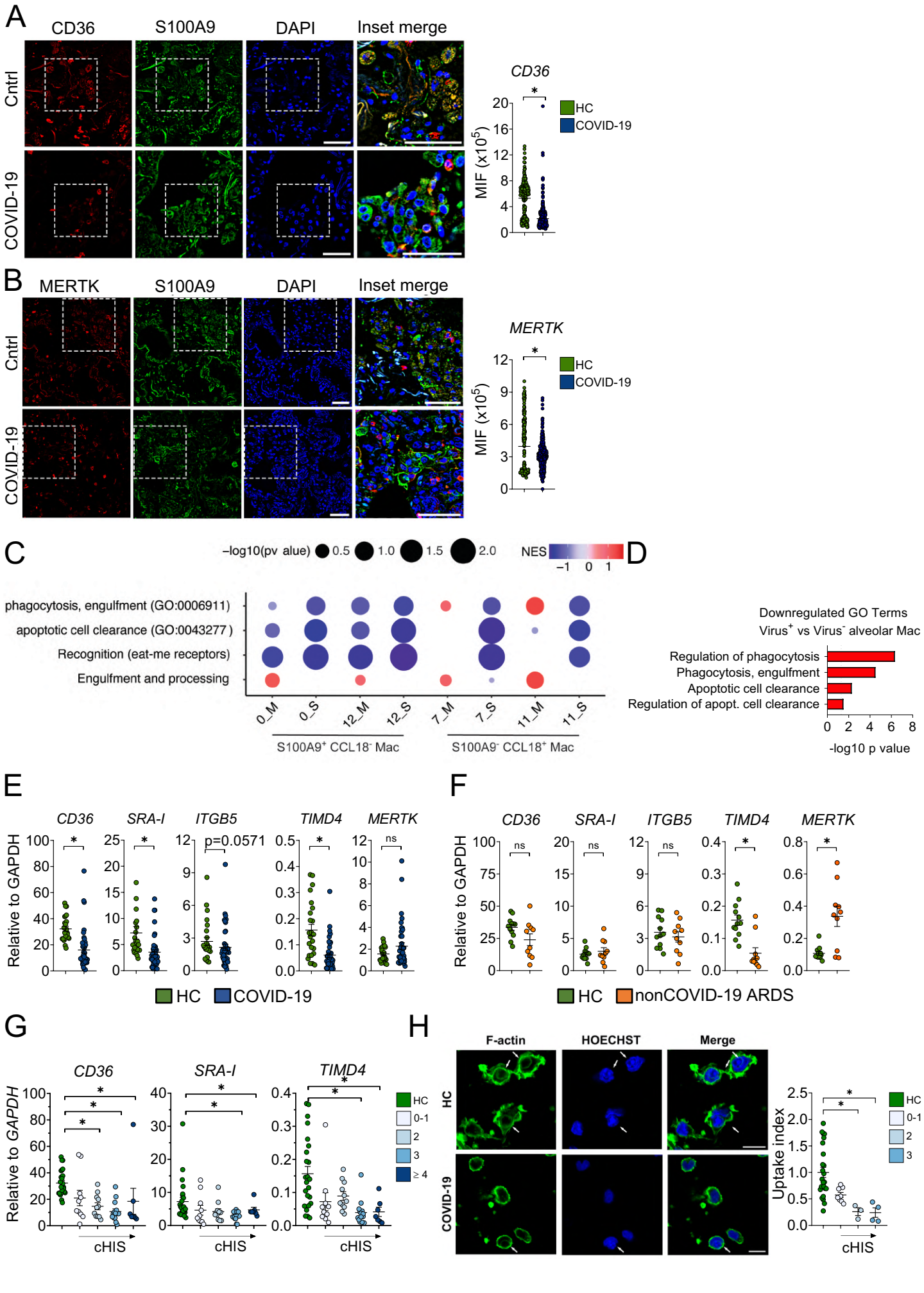

Supplemental Figure 1.

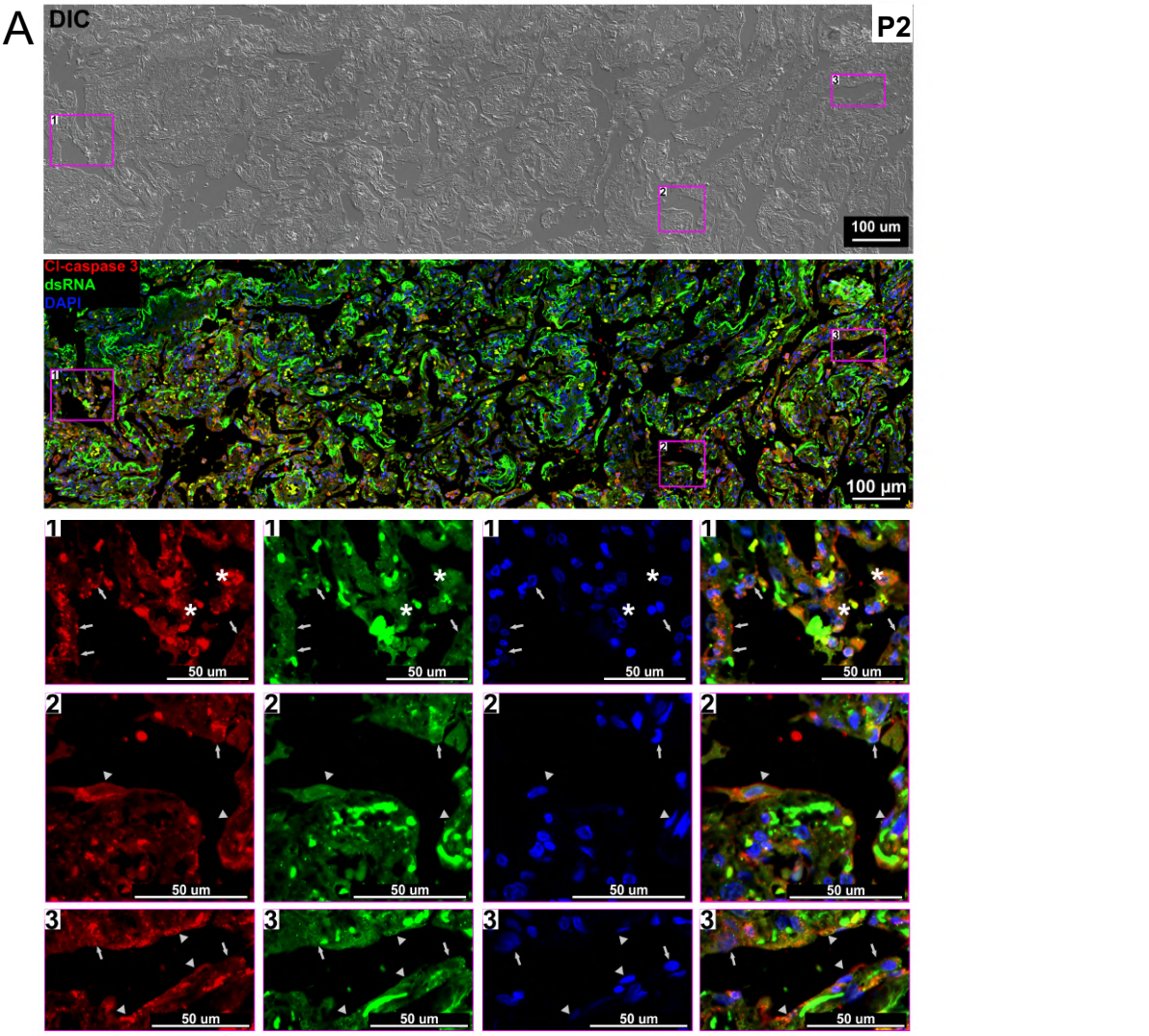

Supplemental Figure 2.

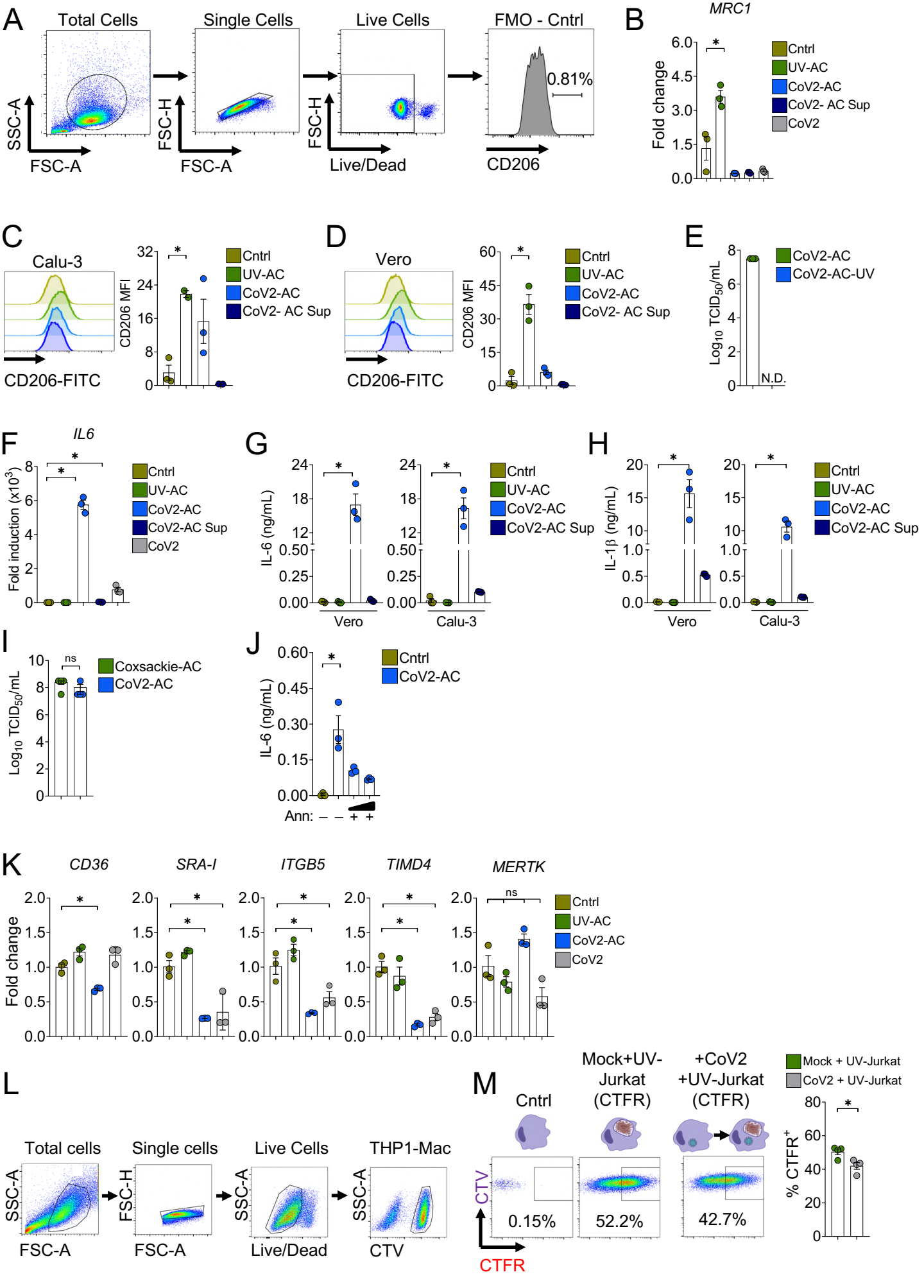

Supplemental Figure 3.

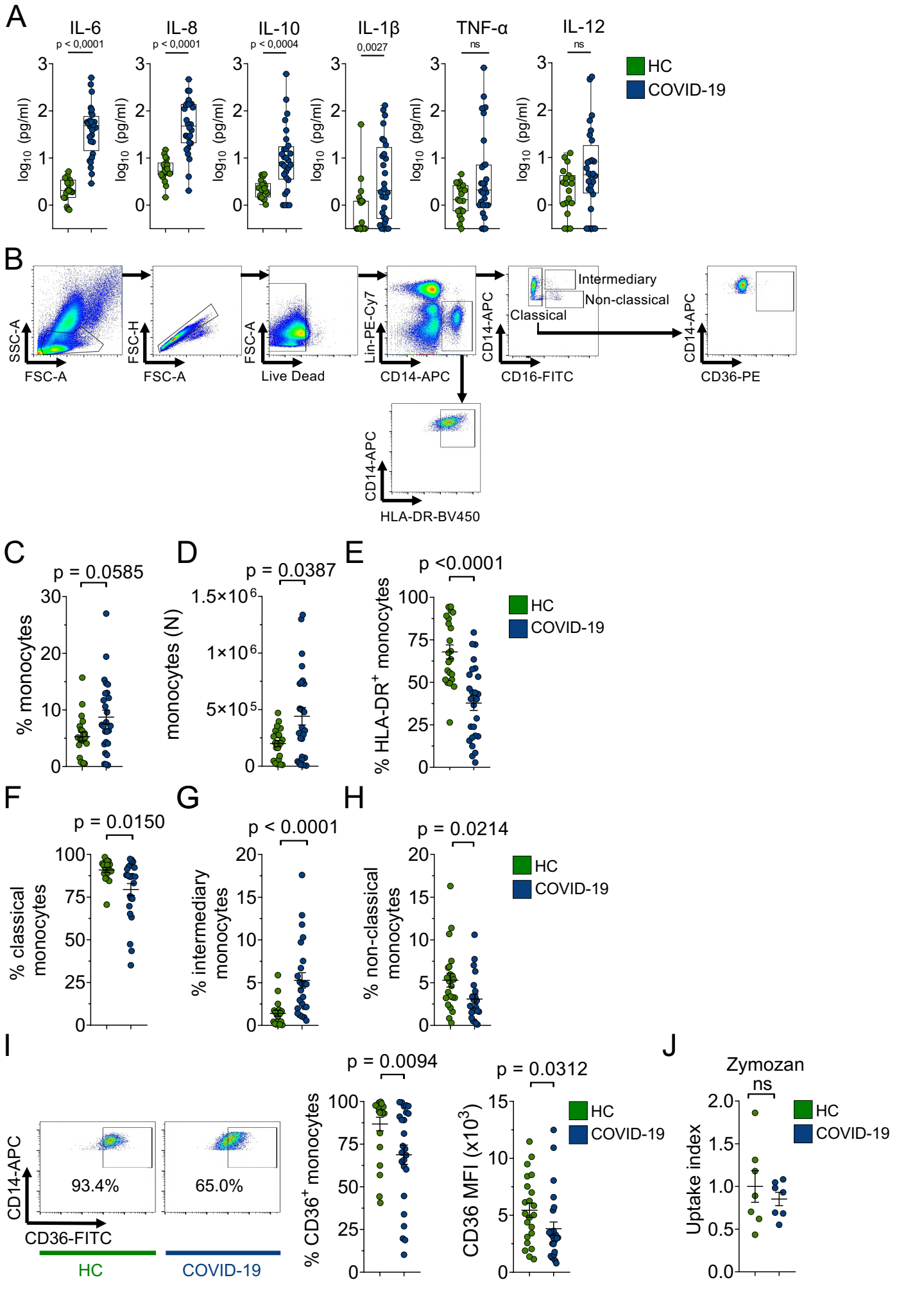

Table S1. Custom gene sets incorporating genes associated to efferocytic pathways and related to human diseases (Penberthy and Ravichandran, 2016; Boada-Romero et al., 2020) (related to Figure 4C).

Term	Gene				
Recognition (eat-me receptors)	GAS6	SCARB1	MARCO	MEGF10	STAB1
	MERTK	ITGB3	MFGE8	MSR1	STAB2
	ADGRB1	ITGAV	AXL	TIMD4	AGER
	LRP1	CD36	TYRO3	C1QA	SCARF1
Engulfment and processing	RAC2	RHOBTB1	DNM1L	ABCA1	ATG7
	RAC1	RHOG	ELMO1	RUBCN	ATG16L1
	RHOH	RAB14	SLC2A1	BECN1	GULP
	TREX1	TYROBP	SLC12A4	PIK3C3	
	RHOBTB2	DOCK1	DNASE2	ATG5	

Table S2. Medical characteristics of COVID-19 patients

	Demographics	%
Number	60	
Age	61.48 ± 16.07	
Female		43.3
	Comorbidities	
Hypertension	35	58
Obesity	32	57
Diabetes	22	37
History of smoking	8	15
Heart disease	16	27
Lung disease	11	18
Kidney disease	8	14
Cancer	6	10
History of stroke	1	2
Immunodeficiency	1	2
Autoimmune diseases	2	3
	Laboratorial findings	
CRP (mg/dL)	11.78 ± 8.09	
D-Dimers (µg/mL)	3.30 ± 3.15	
LDH (U/L)	855.39 ± 533.04	
Ferritin (ng/mL) of smoking	1494.31 ± 1374.06	
Haemoglobin (g/dL)	12.25 ± 3.35	
Neutrophils (cell/mm3)	8004.18 ± 5026.49	
Lymphocytes (cell/mm3)	1572.42 ± 1098.80	
Platelets (count/mm3)	251066.67 ± 105331.26	
	Medications	
Heparin	58	97
Antibiotics	56	93
Glucocorticoids	57	95
Oseltamivir	14	25
Antimalarial	2	4
	Respiratory status	
Mechanical ventilation	42	70
Nasal-cannula oxygen	60	100
pO2	79.87 ± 35.53	
SatO2	91.84 ± 9.90	
	Disease severity	
Mild	0	0
Moderate	10	17.24
Severe	50	86.21
	Outcome	
Death	27	46.55

*CRP: C-reactive protein (normal value <0.5 mg/dl); **D-dimers (normal value <0.5 µg/ml); :

#LDH: lactate dehydrogenase (normal range: 120–246 U/liter); &Ferritin (normal range: 10-291 ng/ml)

Table S3. Medical characteristics of nonCOVID-19 ARDS patients

	Demographics	%
Number	10	
Age	67.10 ± 12.04	
Female		40
	Comorbidities	
Hypertension	8	80
Obesity	4	40
Diabetes	6	60
History of smoking	7	70
Heart disease	6	60
Lung disease	5	50
Kidney disease	2	20
Cancer	2	20
History of stroke	1	10
Immunodeficiency	1	10
Autoimmune diseases	0	0
	Laboratorial findings	
CRP (mg/dL)*	8.82 ± 10.29	
D-Dimers (µg/mL)**	4.69 ± 3.69	
LDH (U/L)#	1700.22 ± 2542.49	
Ferritin (ng/mL)&	N.D.	
Haemoglobin (g/dL)	15.00 ± 4.74	
Neutrophils (cell/mm3)	9300.00 ± 4998.67	
Lymphocytes (cell/mm3	2070.00 ± 1418.18	
Platelets (count/mm3)	222300.000 ± 116946.38	
	Medications	
Heparin	9	90
Antibiotics	9	90
Glucocorticoids	6	60
Oseltamivir	1	10
Antimalarial	0	0
	Respiratory status	
Mechanical ventilation	7	70
Nasal-cannula oxygen	10	100
pO2	71.27 ± 18.18	
SatO2	91.55 ± 7.73	
	Disease severity	
Mild	0	0
Moderate	1	10
Severe	9	90
	Outcome	
Death	7	70

*CRP: C-reactive protein (normal value <0.5 mg/dl); **D-dimers (normal value <0.5 µg/ml); :

#LDH: lactate dehydrogenase (normal range: 120–246 U/liter); &Ferritin (normal range: 10-291 ng/ml)